THE JOURNAL OF PHYSICAL CHEMISTRY C

Article

Electronic Structure of the Perylene / Zinc Oxide Interface: A Computational Study of Photoinduced Electron Transfer and Impact of Surface Defects

Jingrui Li, Hong Li, Paul Winget, and Jean-Luc Bredas

J. Phys. Chem. C, **Just Accepted Manuscript** • DOI: 10.1021/acs.jpcc.5b03596 • Publication Date (Web): 29 Jul 2015

Electronic Structure of the Perylene / Zinc Oxide Interface: A Computational Study of Photoinduced Electron Transfer and Impact of Surface Defects

Jingrui Li,[†,¶] Hong Li,[†] Paul Winget,[†] and Jean-Luc Brédas[*,†,‡]

School of Chemistry and Biochemistry, Center for Organic Photonics and Electronics, Georgia Institute of Technology, Atlanta, GA 30332-0400, USA, and Solar and Photovoltaics Engineering Research Center, King Abdullah University of Science and Technology - KAUST, Thuwal 23955-6900, Kingdom of Saudi Arabia

E-mail: jean-luc.bredas@kaust.edu.sa

[*]To whom correspondence should be addressed

[†]School of Chemistry and Biochemistry, Center for Organic Photonics and Electronics, Georgia Institute of Technology, Atlanta, GA 30332-0400, USA

[‡]Solar and Photovoltaics Engineering Research Center, King Abdullah University of Science and Technology - KAUST, Thuwal 23955-6900, Kingdom of Saudi Arabia

[¶]Current address: Department of Applied Physics and Centre of Excellence in Computational Nanoscience, Aalto University School of Science, P.O.Box 11100, FI-00076 AALTO, Finland

Abstract

The electronic properties of dye-sensitized semiconductor surfaces consisting of perylene chromophores chemisorbed on zinc oxide via different spacer-anchor groups, have been studied at the density-functional-theory level. The energy distributions of the donor states and the rates of photoinduced electron transfer from dye to surface are predicted. We evaluate in particular the impact of saturated versus unsaturated aliphatic spacer groups inserted between the perylene chromophore and the semiconductor as well as the influence of surface defects on the electron-injection rates.

Introduction

Zinc oxide (ZnO) represents a promising transparent conductive oxide with the potential for widespread use in both inorganic and organic optoelectronic devices, for example, as active elements of sensors and lasers[1] and more recently as nanostructured electrodes in hybrid photovoltaic cells[2,3]. ZnO has also been exploited as a hole-blocking / electron-selective interlayer between an indium-tin-oxide electrode and an organic electron-transport active layer in organic light-emitting diodes[4–9] as well as in organic solar cells with inverted device architectures[10–27]. In all these applications, charge injection at the interface between ZnO and an (organic) active layer is a critical process controlling device performance.

Over the past decade, ZnO has also received increasing attention as an electrode material in nanostructured dye-sensitized solar cells (DSSCs)[28–32]. In such devices, the photoinduced electron-transfer (ET) reactions at the dye-semiconductor interface, in particular the processes of electron injection from an electronically excited state of a chemisorbed dye molecule into the semiconductor substrate, represent a key step for photonic energy conversion[33–38]. In recent years, photoinduced ET processes in dye-semiconductor systems have been studied in great detail experimentally with femtosecond spectroscopy techniques[34,35,37,39–56]. It has been shown that electron-injection processes at the dye-semiconductor interfaces often take place on an ultrafast sub-picosecond timescale[37,43,45,46,57,58]. In comparison to the most commonly

considered titanium-dioxide-based DSSCs, ZnO has the advantage of high electron mobility, which leads to faster electron transport in the electrode and thus a higher efficiency of charge separation. In addition, recent developments in the synthesis of ZnO nanomaterials have led to a wide variety of ZnO nanostructures for DSSCs[31,59,60].

A theoretical study of interfacial ET reactions requires a quantum-mechanical description of the processes, which includes electronic-structure characterizations of the systems and simulations of the ET dynamics[61–64]. To this end, a variety of methods have been developed and applied[65–103]. The electronic structure of dye molecules adsorbed on semiconductor substrates has been studied by employing cluster models for nanoparticles[74,77,79,80,88,92,104] or a slab model with periodic boundary conditions as an extended surface[75,78,82–85,101,103,105–107]. Information from the electronic-structure calculations has been used to determine the interfacial electronic coupling strengths, which play the key role in the dynamical simulations. The dynamics of electron injection at dye-semiconductor interfaces has been studied with first-principles simulations[82–84,86–90] as well as models based on parametrized Hamiltonians[65–73,81,91,93–95]. The former class of dynamical methods typically use mixed-quantum-classical approaches to treat the nuclear dynamics, such as the classical path or Ehrenfest method[63,90,103,108] and the surface-hopping approach[108–110]. In contrast, the model-based approaches often allow a numerically exact, fully quantum-mechanical treatment of the ET dynamics[65–72,91,92].

In this work, we present a theoretical study of perylene chromophores chemisorbed via a carboxylic-acid anchor group on the surface of zinc oxide with a wurtzite structure. These systems allow a direct comparison with results of ultrafast laser spectroscopy experiments for the related dye molecules (with 2,5-di-*tert*-butyl substitution) on the ZnO surface[52,56], where the rates of interfacial ET were reported to occur on a sub-picosecond timescale. The electronic structure of one of the considered systems, perylene-acrylic acid / ZnO, was studied in an earlier work based on a cluster model for zinc oxide nanoparticles[104]. Here, we employ a slab model with periodic boundary conditions to describe extended surfaces of the oxide semiconductor in electronic-structure calculations based on density functional theory (DFT). This can

be regarded as the first step of the approach to the ET dynamics. Based on the electronic-structure results, we are able to predict some important features of the heterogeneous ET, including the rate, the possible incompleteness of ET, as well as the extent of coherence effects.

A major focus of our study is the influence of nature of spacer groups. In particular, we consider the effects of saturated and unsaturated aliphatic spacer groups inserted between the perylene chromophore and the carboxylic-acid anchor group. Earlier theoretical studies on the photoinduced ET between the same dye molecules and TiO_2 surfaces have revealed an apparent dependence of ET on the spacer groups[99]. Although bulk ZnO and TiO_2 possess similar band energetics[38,111], their band structure differ from each other in many aspects. In particular, the much lower density of states of the bottom of the conduction band due to the 4s-character in ZnO (the conduction band in TiO_2 consists of major contributions from the Ti-3d orbitals) is expected to play a major role in the interfacial ET.

In addition, surface defects have significant impacts on the electronic structure of ZnO[112], which has motivated us to investigate their effects on the interfacial electronic structures and the charge-transfer dynamics. Previous experimental[113–117] and theoretical[112,118–127] studies have indicated that surface defects, such as oxygen-vacancies, zinc-vacancies, zinc-interstitials, and their combinations, have significant impact on the electronic structure of ZnO. Here, we consider two different surface defects: an oxygen-vacancy located in the topmost ZnO-layer, and a zinc-interstitial inserted in a deeper location. Both types of defects correspond to the zinc-rich limit of ZnO and have been suggested as possible origins of the n-type conductivity in ZnO. Our study provides a way of modulating the ET dynamics by varying the electronic structure of both the dye adsorbate and the semiconductor substrate. A systematic study on the effects of defects on the ET requires further surface modeling of ZnO, not only by considering more types of defects and their combinations, but also by varying their relative locations with respect to the surface adsorption site. Such a topic is beyond the scope of this paper and will be studied in future work.

Model systems and computational methods

Characterization of investigated systems

We study two organic molecules (depicted in Figure 1), which have been recently investigated in great detail experimentally as photo-sensitizers of semiconductor surfaces:[40,50–52,56,80] perylene-9-yl-prop-9-enoic acid (denoted by **1** for simplicity) and perylene-9-yl-propionic acid (denoted by **2**). Both dye molecules contain a perylene chromophore group and a carboxylic-acid anchor group. They differ from each other by the spacer group: an unsaturated -CH=CH- group for **1** (perylene-acrylic acid) and a saturated -CH_2CH_2- group for **2** (perylene-propionic acid). As a result of the nonrigid saturated aliphatic spacer group, two adsorption geometries of dye **2** at the ZnO surfaces are included in the study, one with the perylene plane nearly perpendicular to the ZnO polar surface and the other with the perylene plane nearly parallel to the surface (with the adsorbate in the latter cases denoted by **2′)**. The adsorption energy of **2** on the polar ZnO surface is about 0.5 eV larger than for **2′**.

The first-principles DFT calculations for each complex are based on a slab model and adopt an orthogonal supercell with dimensions $a = 13.000$ Å, $b = 11.259$ Å and $c = 52.071$ Å in the $[2\bar{1}\bar{1}0]$, $[01\bar{1}0]$ and $[0001]$ directions of the ZnO (wurtzite) structure, respectively. The lattice parameters a and b were derived from the primitive lattice parameters obtained from powder-neutron-diffraction structure[128]; c was chosen to ensure a vacuum space with a thickness larger than 24 Å. Following the indications gained in our previous work[112], for each system, a hydroxylated zinc-terminated (0001) polar surface of ZnO is modeled (referred as model **a**) by a repeating slab consisting of six Zn-O double layers, each composed of 16 zinc and 16 oxygen atoms. In each complex, a perylene chromophore was bound to the ZnO surface via the deprotonated carboxylic anchor group in a bidentate (bridge) mode, thus mimicking a dehydration reaction between the adsorbate and a hydroxyl group on the surface. The dangling bonds of other surface zinc atoms were saturated by hydroxyl groups with a $\frac{1}{2}$ monolayer coverage. Furthermore, the dangling bond of each oxygen atom in the bottommost layer

was saturated by an "artificial hydrogen atom" with a nuclear charge of $+\frac{1}{2}$ e and an electron charge of $-\frac{1}{2}$ e[112]. This termination of surface dangling bonds together with the application of a thick vacuum layer (thickness $>$ 24 Å) and the dipole correction[129] avoid the danger of artificial interactions between the slabs. Also interaction among neighboring adsorbates are significantly reduced due to the relatively large surface area per unit cell.

We also consider two defect-containing models (**b** and **c**) created based on model **a**. Model **a** represents a fully hydroxylated zinc-terminated (0001) polar surface and does not contain any intrinsic defects such as vacancies and interstitials of oxygen or zinc. Model **b** contains an isolated oxygen vacancy obtained by removing an oxygen atom bridging two surface zinc atoms. Model **c** contains an interstitial zinc atom which is inserted at an octahedral site between the second and third Zn-layers. For the complex with the ZnO surface of model **b**, the perylene chromophore is anchored to the zinc atoms where the bridging oxygen atom is removed; for the complex with surface of model **c**, the dye adsorbate is located on the surface so that the distance between it and each of the four nearest interstitial zinc atoms is nearly identical. These defect-containing surfaces have been extensively discussed in our previous work[112].

The relaxed structures of the perylene adsorbed on the fully hydroxylated surface model **a** are depicted in Figure 2. They are denoted in the following by **1-a**, **2-a** and **2′-a**, respectively. The complexes with defect-containing surfaces, models **b** and **c**, are denoted accordingly by **1-b**/**c**, **2-b**/**c** and **2′-b**/**c**. Their relaxed structures are depicted in Figure 3.

In the course of geometry optimization, the adsorbate and the top three Zn-O-layers were relaxed (including the surface hydroxyl groups), while the bottom three Zn-O-layers were frozen at their positions according to the experimental ZnO wurtzite structure[128]. All DFT calculations were performed with the Vienna *Ab initio* Simulation Package (VASP)[130–132] in the same way as in our previous work[112] to insure consistency of the results. The plane-wave cutoff was set to 400 eV. The Perdew-Burke-Ernzerhof (PBE) generalized gradient approximation (GGA) was used as the exchange-correlation functional[133] in combination with the projector-augmented

wave (PAW) method[134] to describe the interactions between the core-ions and valence electrons. The GGA+U approximation[135] was adopted to describe the on-site Coulomb interaction among the localized 3d electrons of zinc atoms. The effective Hubbard U-parameter for the zinc-3d electrons was set to 8.5 eV, which places the Zn-3d band 7.7 eV below the valence-band maximum (VBM) in the bulk of ZnO-wurtzite[112,136] in accordance to the experimental result[137]. A $2 \times 2 \times 1$ k-mesh was used for the Brillouin-zone integrations in the geometry optimization, while for the self-consistent electronic-structure calculations a $4 \times 4 \times 1$ k-mesh was used.

Analysis of interfacial electronic interaction and simulation of ET dynamics

To analyze the electronic interaction and to estimate the rate of electron injection from a photoexcited state of the dye adsorbate into the semiconductor substrate, we employed a model Hamiltonian which is represented in a basis of diabatic (charge-localized) electronic states which are relevant for the ET process: the donor state ψ_{d} (each corresponding to the product of an electronically excited state of the bound dye and an empty conduction band of the semiconductor in the limit of vanishing dye-semiconductor coupling) and the continuum of acceptor states $\{\psi_k\}$ (corresponding to the product of the ground state of the adsorbate-cation and a conduction-band state in the zero-coupling limit). Accordingly, the Anderson-Newns type ET Hamiltonian[138,139] can be written as

$$\hat{H} \triangleq |\psi_{\mathrm{d}}\rangle E_{\mathrm{d}} \langle\psi_{\mathrm{d}}| + \sum_k |\psi_k\rangle E_k \langle\psi_k| + \sum_k (|\psi_{\mathrm{d}}\rangle V_k^{\mathrm{da}} \langle\psi_k| + \text{c.c.}). \quad (1)$$

Here, E_{d} and E_k denote the energies of the electronic donor and the kth electronic acceptor state, respectively. The offdiagonal matrix elements $\{V_k^{\mathrm{da}}\}$ characterize the donor-acceptor coupling and c.c. stands for complex conjugate. In the present study, we have not fully considered the coupling to the vibrational motions due to the technical complexity present when

using adiabatic states (charge-delocalized eigenstates) as basis states (see more details in the discussion following Eq. 6). Instead, as an estimation of the vibronic effects on the electron-transfer dynamics, we have simulated the ET dynamics in some of the investigated systems by including essential vibrational modes (see details in Section 2.1 in the Supporting Information). These simulation results indicated that indeed a more thorough account of these effects should be considered in a separate future work.

There are various methods to define the ET-relevant diabatic states and to obtain the parameters in Eq. 1, such as by employing semiempirical models[73,88,91,92], by calculating the width of energy distribution of the donor state[79,80] and by employing a first-principles-based method following the projection-operator approach[96]. Here, we make use of the scheme of density-of-states (DOS) of the overall system as well as the scheme of projected DOS (PDOS) on some particular components to analyze the interfacial electronic interaction. The PDOS projected onto the dye (simply written as dye-PDOS in the following) plays a particularly important role in the simulation of electronic transition from an initial state localized on the dye adsorbate to a group of states localized on the semiconductor-substrate. In principle, the energy distribution of the donor state, which can be obtained from the dye-PDOS scheme, contains all required information about the donor-acceptor coupling and can be directly used to simulate the dynamics of electronic transition at the purely electronic level. The approach introduced in this section, which is based on the slab electronic-structure calculations, goes beyond the closely related energy-broadening analysis[79,80]; it also shows similarity to the extended-Hückel approach[88] in the construction of the initial (donor) state as well as the dynamical simulation; furthermore, it can be mathematically transformed into the previously proposed first-principles-based approach[96] which employs a partitioning scheme to define the donor and acceptor subspaces and to obtain the ET-Hamiltonian matrix elements based on the cluster electronic-structure calculations.

We work here within the mean-field single-electron picture. Thus, in the effective ET Hamiltonian we use the orbitals and orbital energies to represent the corresponding system states

and energies. Both electron-injection processes from the S_1 and S_2 excited states of the adsorbed dye molecule (termed hereafter as dye-S_1 and dye-S_2, respectively) have been considered in order to simulate the interfacial ET after photoexcitation as well as that after 2-photon excitation. These donor states are represented in the single-electron picture by the two lowest unoccupied orbitals localized on the dye adsorbate, which are associated with the lowest unoccupied molecular orbital (LUMO) and the (LUMO+1) of the corresponding isolated dye molecule and referred to as dye-LUMO and dye-(LUMO+1), respectively. The orbital localized on the adsorbed dye which is associated to the highest occupied molecular orbital (HOMO) of the corresponding isolated dye molecule is termed dye-HOMO. Time-dependent DFT calculations for the dye molecules considered here indicate that the first and second excited states are almost exclusively corresponding to the HOMO-LUMO and HOMO-(LUMO+1) excitation, respectively. Accordingly, these schemes can be obtained from well-converged periodic (slab-model) electronic-structure calculations of high accuracy.

As a first step, we relate the donor state ψ_d to the dye-PDOS within a certain energy region. For a donor state which is energetically well-separated from other states localized on the dye adsorbate, this can be done, *e.g.*, by comparing its energy and a well-defined reference energy, such as the Fermi energy or the HOMO of the overall system, or based on the distribution of charge density. The donor-state energy at the equilibrium geometry, ε_d, can be immediately determined from the thus obtained energy distribution function of the donor state, $\rho_\mathrm{d}(\epsilon)$, by:

$$\varepsilon_\mathrm{d} = \frac{\int \epsilon \rho_\mathrm{d}(\epsilon)\,\mathrm{d}\,\epsilon}{\int \rho_\mathrm{d}(\epsilon)\,\mathrm{d}\,\epsilon}. \tag{2}$$

In a practical approach, we can properly discretize the continuous $\rho_\mathrm{d}(\epsilon)$-function into a set of data pairs $\{(c_n, \epsilon_n) \mid n = 1, 2, \cdots, N\}$ satisfying:

$$\varepsilon_\mathrm{d} = \sum_{n=1}^{N} |c_n|^2 \epsilon_n, \quad \sum_{n=1}^{N} |c_n|^2 = 1. \tag{3}$$

The energy distribution given by Eq. 2 or 3 indicates the possible outcomes of an one-electron

energy measurement in the system prepared in the donor state and the associated probabilities. Accordingly, the donor state ψ_{d} can be represented as a linear combination of eigenstates of the one-electron Hamiltonian (MOs) of the overall system:

$$\psi_{\mathrm{d}} = \sum_{n=1}^{N} c_n \phi_n \tag{4}$$

where the energy of the eigenstate ϕ_n is ϵ_n.

Within the eigenstate representation, the Hamiltonian operator is represented by a real diagonal matrix containing the eigenvalues as diagonal entries, and the time-dependent wavepacket is represented as a linear combination of eigenstates:

$$\Psi(t) = \sum_{n=1}^{N} \langle \phi_n | \Psi(0) \rangle \mathrm{e}^{-\mathrm{i}\epsilon_n t} \phi_n. \tag{5}$$

The expansion of ψ_{d}, Eq. 4, shows that the knowledge of a time-dependent wavepacket $\Psi(t)$ for all times is equivalent to the knowledge of all eigenstates $\{\phi_n\}$ and energies $\{\epsilon_n\}$. Thus, from Eq. 3, we can directly calculate the time-evolution of some observables of interest, especially the population of the initial state, at the purely electronic level. Assuming that initially the system is prepared by an ultrashort laser pulse in ψ_{d} , the time-evolution of the initial-state (donor-state) population is given (in atomic units):

$$P_{\mathrm{d}}^{\mathrm{elec}}(t) \triangleq |\langle \psi_{\mathrm{d}} | \mathrm{e}^{-\mathrm{i}\hat{H}t} | \psi_{\mathrm{d}} \rangle|^2 = \left| \sum_{n=1}^{N} |c_n|^2 \mathrm{e}^{-\mathrm{i}\epsilon_n t} \right|^2. \tag{6}$$

Such a dynamical approach, which is often termed as an approach in the "time-independent picture" (as it requires, in general, to solve the time-independent Schrödinger equation instead of the time-dependent one), cannot be straightforwardly extended to the study including the coupling to the vibrational degrees of freedom (DOFs). Especially as the eigenstates (adiabatic states) ϕ_n are usually rather delocalized and have less physical meaning, it is in general difficult to characterize their dependence on nuclear DOFs. In contrast, the diabatic (charge-localized)

states serve as a better basis to expand an electronic-vibrational wavepacket[96,98–100]. Based on the one-dimensional donor-subspace spanned by the donor-state vector defined by Eq. 4, and the acceptor subspace which is the orthogonal complement of the donor subspace, the transformation from the adiabatic to the diabatic representation is straightforward. As we limit our dynamical approach at a purely electronic level, thus not considering the vibronic coupling, we do not outline the detail of the acceptor-space construction, representation transformation, or determination of Hamiltonian matrix elements in Eq. 1.

The computational effort required by the dynamical simulations is reasonable due to the consideration of purely electronic dynamics. When the coupling to the vibrational motion is included, advanced wavepacket-simulation techniques might be required according to the size of the overall system. For example, when only a few (in general < 10) nuclear DOFs are taken into account, a conventional wavepacket-propagation approach suffices to meet the requirement of numerically exact quantum dynamics. For larger systems, as the computational effort grows exponentially with the total number of included DOFs, further improvements to the wavepacket propagation, such as the multiconfiguration time-dependent Hartree (MCTDH) approach[140] and its multilayer formulation[141,142], must be employed towards a numerically exact full-dimensional quantum dynamics, or alternatively, the electronic-nuclear dynamics can also be treated at a mixed-quantum-classical level[143].

Results and discussions

Interfacial energetics and characterization of the ET-relevant states for perylene adsorbed on a fully hydroxylated ZnO surface

To discuss the energy-level alignment of the dye-semiconductor complexes with a fully hydroxylated ZnO surface without defects (model **a**), we first consider their PDOS schemes presented in Figure 4. The PDOS data for the corresponding bare ZnO surface are plotted

as references. All PDOS data were calculated employing a Gaussian smearing method with a width-parameter 0.05 eV and plotted as a function of the energy difference *vs.* the valence-band maximum (VBM) of ZnO.

In all systems, the ZnO-DOS/PDOS (as a sum of the PDOS projected onto the valence orbitals of oxygen atoms in ZnO as well as the Zn-3d- and Zn-4s-PDOS) indicates a continuous DOS scheme. The VBM consists of the occupied O-2p orbitals, while the conduction-band minimum (CBM) is dominated by the Zn-4s orbitals.

For all three dye-semiconductor complexes, the calculated value of band gap is slightly larger than 1.0 eV, which is about 0.2 eV smaller than the band gap of the bare ZnO surface. The band gap of ZnO for all systems shown in Figure 4 is much smaller than the experimental value (3.4 eV[111]) as well as the values calculated using hybrid functionals for ZnO crystals[127,144,145] and the polar ZnO surface[112]. The calculated band gap of the ZnO crystal with GGA+*U* approximation remains 50% lower than the experimental value, a known limitation of the semi-local exchange-correlation functional employed in the standard DFT calculations[127,145]. Further optimization of this parameter and applying a *U* parameter to oxygen atoms would lead to improved band gaps, this would, however, potentially lead to a very system specific treatment. The exchange-correlation dependence on the band structure had been obtained for both the ZnO bulk and different models of ZnO surface[112,127,145]. and shows qualitative agreement with the GGA+*U* treatment applied here. We also have recently demonstrated that HSE06+*U* (a hybrid functional) and PBE+*U* provide similar qualitative descriptions of the electronic structures as a function of the presence of various types of intrinsic and extrinsic ZnO surface defects[112].

Figure 4 shows that the adsorption of the organic dye molecules on the semiconductor surfaces has modified the ZnO band structure in addition to the change of band gap. Some changes in the ZnO-PDOS structures, especially those near the VBM of ZnO, appear upon the adsorption of perylene. In particular, the adsorption of dye **2** with a nearly parallel orientation, as shown in Figure 4(c), introduces a narrow band (with width less than 0.3 eV)

$0.1 \sim 0.2$ eV above the ZnO-VBM. These effects are primarily due to the interaction between the ZnO surface and the adsorbed perylene, as calculations of electron-density distribution (data not shown) indicate that those VBM states are mainly contributed from the oxygen-2p orbitals in the surface hydroxyl groups and the topmost ZnO-layer.

PDOS peaks of the perylene adsorbates in the energy-level alignments reflect significant change in the electronic structure due to the surface adsorption. The PDOS peak corresponding to the dye-HOMO in **1-a** is nearly aligned with the VBM of the ZnO slab, the PDOS peak associated with the dye-HOMO in **2-a** lies above the VBM of ZnO, and the PDOS peak associated with the dye-HOMO in **2′-a** is located < 0.1 eV above the upper edge of the narrow ZnO-band. The energy levels of the lowest unoccupied orbitals of the adsorbed dyes are all located well above the CBM of ZnO. More specifically, in **1-a**, **2-a** and **2′-a**, the dye-LUMO level is 0.5 eV, 0.9 eV and 1.3 eV above the CBM of ZnO, respectively, showing a trend of increased donor (dye-S_1) levels for the three adsorbates.

Both the donor level relative to the CBM as well as the density of the isoenergetic acceptor states (*i.e.*, the acceptor states with energies around the donor level) are important parameters for the ET dynamics. The trend of donor level relative to CBM in **1-a** and **2-a** (given above) is similar to that in the complexes with the corresponding dyes chemisorbed at the titanium-dioxide surface[99]. This corresponds to the similarity of band-structure energies between ZnO and TiO_2. On the other hand, Figure 4 shows a relatively low density of conduction-band states of ZnO, and thus a low density of isoenergetic acceptor states in ZnO. This feature is different from TiO_2, where the density of conduction-band states is much higher in the region near the CBM.

The effects of donor-acceptor coupling on the energy distribution of the donor state, including the broadening and the fine structures, cannot be detected from the peaks associated with the donor states shown in Figure 4 primarily due to the Gaussian smearing. A careful analysis for these donor-state associated peaks has been performed to obtain a more accurate characterization of the donor-acceptor coupling. Test calculations were performed with a

slab exclusively consisting of a layer of dye molecules (*i.e.*, without including the ZnO-layers) with the same molecular geometry (with an optimized position of the hydrogen atom in the carboxylic anchor group) as optimized for the complex and the same unit-cell dimensions. The results indicate negligible intermolecular interactions among the dye adsorbates in the slab. Therefore, we can consider that all broadening and structures of the donor-state energy distribution are due to the donor-acceptor interactions.

Charge-density distributions of complexes **1-a**, **2-a** and **2′-a** corresponding to the dye-HOMO, dye-LUMO and dye-(LUMO+1) levels (as indicated in Figure 4) are illustrated in Figure 5. For the dye-HOMO and dye-LUMO of each system, the resemblance between these projected states and the corresponding MOs of the isolated dye molecules can be observed from a comparison with previous theoretical results, *e.g.*, in Ref. 99. For the simulations of ET dynamics, we focus on the dye-LUMO and dye-(LUMO+1) which are selected as donor states in different ET processes. In **1-a**, where the dye adsorbate almost retains its planar geometry, both dye-LUMO and dye-(LUMO+1) (Figures 5(b) and (c)) exhibit noticeable contribution at the spacer as well as the carboxylic-acid anchor group, as the π-type orbital over the perylene ring is extended by the conjugated alkene spacer group. In contrast, in both dye-LUMO and dye-(LUMO+1) of **2-a** and **2′-a** (Figures 5(e), (f), (h) and (i)), the distribution of electron density over the spacer and the anchor groups are much smaller.

Such local characters of donor states, however, do not necessarily indicate the trend of strengths of donor-acceptor coupling. The pronounced extension of π-orbital over the anchor group in the dye-LUMO of **1-a** creates a smaller distance between the donor-state charge density and the ZnO surface, however, we also notice that the acceptor states around the dye-LUMO in **1-a**, as shown in Figure 5(b), are mainly coming from Zn-4s orbitals in very deep ZnO-layers. This is consistent with the fact that the energetic location of dye-LUMO in **1-a** is close to the CBM[112], which is dominated by charge distributions at the deeper ZnO-layers. Effectively, Figure 5(b) illustrates an “insulating layer” inserted between the charge density of the dye-S_1 state and the acceptor states distributed in the bulk of ZnO substrate. The

thickness of this insulating layer is about 10 Å, thus strongly preventing the electron transfer from perylene to zinc oxide.

In contrast, the acceptor states around the donor level in all other five cases (Figures 5(c), (e), (f), (h) and (i)) show noticeable distributions in both the bulk and the top layers of ZnO. This finding is in accordance with the fact that they are located in the ZnO conduction band well above the minimum, where significant hybridization of the LUMO/LUMO+1 state with the ZnO conduction band is observed. In these five cases, the interaction between the donor and acceptor states with similar energies is expected to be stronger. Such a scheme of acceptor-state charge-density distribution is expected to be favorable to both electron injection from the dye adsorbate to the semiconductor surface as well as the subsequent charge transport within the bulk of the semiconductor.

The calculated HOMO-LUMO excitation energies of dyes **1** and **2** adsorbed at the hydroxylated ZnO surface are 1.65 eV and 1.83 eV, respectively. Both values are about 1 eV smaller than the previous theoretical results for corresponding isolated and bound molecules calculated using hybrid functionals[80,99]. The difference between these two HOMO-LUMO excitation energies agrees with previous results[80,99]. The underestimation of both HOMO-LUMO gap of dye (for about 1 eV) and the band gap of the semiconductor (for about 2 eV) is due to the DFT calculations at the GGA level. We have performed test calculations using PBE, a GGA functional, and B3LYP, a hybrid functional, for the considered isolated dye molecules. The results show that: for dye **1**, the HOMO level obtained using GGA is 0.79 eV higher than the B3LYP result, and the GGA-LUMO level is 0.30 eV lower; for dye **2**, GGA calculation results in a 0.74 eV higher HOMO level, while the GGA-LUMO level is 0.42 eV lower than the B3LYP result.

The alignment of frontier orbital energies with the substrate band edges is a central issue in the electronic structure of hybrid interfaces and one of the decisive factors in the interfacial charge transfer considered in this paper. In principle, highly accurate quantum chemistry methods are required for a fully quantitative understanding of the band alignment at organic

interfaces, since the use of Kohn-Sham energy levels, especially from DFT calculations at the GGA level, can lead to errors in this alignment[146–148]. However, the very large size of the unit cells for the combined interface (for example, 261 atoms in **1-a**) precludes the use of *GW*[149] or G_0W_0 methods in the calculations for ZnO, defect-containing ZnO and perylene derivatives.

As described in the computational methods section, we have adopted the GGA+*U* method to correct the shortcomings of DFT, where the self-interaction error in DFT methods is partially accounted for by an effective Hubbard *U*-parameter to describe the on-site Coulomb interaction among the localized zinc 3d electrons. We believe that this approach can be relied on to calculate the properties of hybrid interfaces considered in this paper, since (i) image potential and polarization effects at the interfaces tend to fortuitously cancel the self-interaction corrections, and (ii) our recent study[112] indicated that the CBM of the hydroxylated zinc-terminated (0001) surface calculated by GGA is 0.45 eV lower than the result obtained using the hybrid HSE06 functional, while the GGA-result for the VBM is 0.93 eV higher than the VBM calculated by HSE06. While DFT calculations at the GGA level underestimate the dye-HOMO level position relative to the semiconductor-VBM, the shift of dye-LUMO *vs.* CBM is much smaller, indicating a consistent shift of the dye-LUMO/CBM alignment. This lends confidence in the reliability of the trends in electron-transfer dynamics discussed in the present work. Electronic-structure (DFT) calculations at a higher level by employing, *e.g.*, hybrid functionals[112,136] or the *GW*-approximation[149], however, is an interesting topic of future work.

Interfacial energetics and characterization of the ET-relevant states for perylene adsorbed on defect-containing ZnO surfaces

Figures 6 and 7 show the PDOS schemes of complexes consisting of an oxygen-vacancy containing ZnO (model **b**) and a zinc-interstitial containing ZnO (model **c**), respectively. The PDOS data for the corresponding bare ZnO surfaces are also plotted. (The details of the calculations and plotting of these PDOS data are identical to those for the complexes with

ZnO surfaces of model **a** as mentioned previously).

As shown in Figures 6 and 7, the ZnO-DOS/PDOS indicates a DOS scheme with the chemical nature of both VBM and CBM states similar to those of the hydroxylated ZnO surface, while the adsorption of organic dye molecules introduces modifications of the ZnO band structure. Here, we focus on the effects of defects on the interfacial electronic structure as well as the character of the ET-relevant states. These include the modification of the ZnO band structure, the shift of dye-LUMO and dye-(LUMO+1) levels with respect to the CBM, and the varying local characters of acceptor states around the corresponding donor levels.

For oxygen-vacancy containing systems, the calculated band gap is 1.2 eV, which is about 0.2 eV larger than the value obtained for the systems with a hydroxylated ZnO surface calculated with the same methodology. Similar to the systems with the ZnO surface of model **a**, the adsorption of perylene also leads to a decrease of the ZnO band gap by about 0.3 eV. In this model, the oxygen-vacancy defect introduces a fully occupied deep donor level (labeled by $*$ in Figure 6) in the band gap. The corresponding electron-density distribution, depicted in Figure 8, illustrates that the charge density of this "oxygen-vacancy state" is mainly coming from the 4s orbitals of zinc atoms surrounding the oxygen-vacancy and the 2p orbitals of oxygen atoms bound to the surrounding Zn atoms. The energy of the "oxygen-vacancy state" is located at 0.2 eV (in both **1**- and **2-b**) or 0.4 eV (in **2′-b**) below the CBM. This resembles the result that the oxygen-vacancy level is located right below the CBM as reported in an earlier study for the bare ZnO surface[112], while a much larger gap ($\sim$ 1 eV) between the oxygen-vacancy level and the CBM was obtained for oxygen-vacancy containing ZnO crystal by other groups[120,122,123].

The PDOS-schemes at the HOMO level of both complexes **1**- and **2-b**, as shown in Figures 6(a) and (b), are nearly identical (in both shape and position) to those of **1-** and **2-a** (Figures 4(a) and (b)). The PDOS peak corresponding to the dye-HOMO in **1-b** is nearly aligned with the VBM of ZnO, while the PDOS peak associated with the dye-HOMO in **2-b** is well separated from the VBM. The effect of oxygen-vacancy on the alignment of the dye-PDOS

with respect to the band edges of ZnO in **2′-b** is slightly different from the other two systems. As shown in Figure 6(c), there is an overall shift of -0.1 eV of dye-PDOS scheme as compared with reference system **2′-a** (Figure 4(c)). This small effect is attributed to the location of the oxygen-vacancy in the topmost ZnO-layer, where the narrow ZnO-band is distributed.

The energy levels of the lowest unoccupied orbitals of the dyes, on the other hand, are located above the CBM. For dyes **1** and **2** adsorbed on the ZnO surface of model **b**, the calculated HOMO-LUMO gaps are 1.66 eV and 1.83 eV, respectively. Both values are nearly identical to the results obtained for systems with a hydroxylated ZnO surface. For both dye-LUMO and dye-(LUMO+1) levels, the energy differences to the CBM are smaller than the values for the corresponding dye-**a** systems. This is due to the conduction-band shift towards higher energy caused by the oxygen-vacancy. Figure 6 indicates a relatively low density of isoenergetic acceptor states for the dye-LUMO in all three dye-**b** systems.

The removal of an oxygen atom has left extra valence (4s) electrons on the surrounding zinc atoms, which are interacting with the 2p σ-type electrons of both oxygen atoms in the carboxylic-acid anchor group. The charge-density distribution of the "oxygen-vacancy state" retains a rather localized character around the site of the removed oxygen. Its effects on the energy levels of the π-type dye-HOMO, dye-LUMO and dye-(LUMO+1) are small.

The effects of oxygen-vacancy on the donor-acceptor interactions can be analyzed based on the charge-density distribution of isoenergetic acceptor states (Figure 9). In addition to the spatial character of acceptor states shown in the corresponding dye-**a** systems (Figure 5), there is apparent contribution from the cavity around the position of the removed oxygen. This effect could be especially important in the ET systems when selecting the dye-LUMO as the donor state, since Figure 9 indicates that the oxygen-vacancy favors the extension of charge density to the top ZnO-layers. The charge density of acceptor states around the dye-(LUMO+1) level for each dye-**b** system exhibits a pronounced spatial distribution over the ZnO-layers near the dye-semiconductor interface with a significant increase around the oxygen-vacancy.

In the case of the zinc-interstitial containing system, the VBM-CBM gap is 1.5 eV, which is

larger than in model **a** or **b**. The adsorption of perylene at the ZnO surface of model **c** hardly changes the ZnO band gap. However, note that in this case the Fermi level is 0.8 eV above the CBM, indicating that the system is degenerately doped; an optical gap of 2.3 eV should then be expected due to the Burstein-Moss effect. The zinc-interstitial leads to a system-dependent positive shift of the dye-HOMO level *vs.* VBM: 0.9 eV, 0.5 eV and 0.1 eV for **1-**, **2-** and **2′-c**, respectively. Also, the lowest unoccupied orbitals of the dyes shift in parallel and are located well above the CBM. Interestingly, the LUMO of the three dye molecules are all partially occupied and aligned with the Fermi level of the interfaces. This difference is in particular notable in **1-c** as the dye-LUMO level is located well above the CBM. The calculated HOMO-LUMO excitation energy of the adsorbed dye **1** on the ZnO surface of model **c** is 1.47 eV, which is nearly 0.2 eV smaller than the corresponding value obtained for both models **a** and **b**. Such a red-shift of HOMO-LUMO excitation indicates a stronger interaction between the dye-LUMO and the conduction band. In contrast, the HOMO-LUMO gaps of both **2-c** and **2′-c** are very close to the values for the corresponding systems with surface models **a** and **b**.

In contrast to the oxygen-vacancy close to the surface, the zinc atom inserted between the second and third Zn-layers does not introduce any particular states within the band gap (Figure 7). The effects of zinc-interstitial on the electronic structure of ZnO are rather due to its modification on the conduction-band states especially those near the CBM. The results of DFT calculations, especially the Fermi levels (as indicated in Figure 7), indicate that these states are partially occupied, which is naturally related to the valence (4s) electrons of the inserted zinc atom. Figure 10 illustrates the charge-density distribution at the CBM of **1-**, **2-** and **2′-c**. We notice that these CBM states do no longer exhibit a character of distribution over the deep ZnO-layers. On the contrary, the valence electrons originating from the inserted zinc atom are rather delocalized over the second and the third (0001) Zn-layers, thus leading to a metallic character in these systems[112]. This finding supports the suggestion of the zinc-interstitial defect being one of the major origins of the unintentional n-type doping.

Similar to the results of our previous study[112], these occupied states at the CBM drive the

valence band of ZnO towards a lower energy thus increasing the band gap. The feature that the energy-distribution of the PDOS projected onto the zinc-interstitial is not limited around the CBM but rather spreads over a large energy region in the conduction band, as reported in Ref. 112, is reproduced by the charge-density distribution plots: the isoenergetic acceptor states in the ET systems with a model-**c** ZnO surface, as illustrated in Figures 11(b), (c), (e), (f), (h) and (i), which are energetically well above the CBM (*cf.* Figure 7), exhibit significant distributions in both top ZnO-layers and bulk of ZnO.

Electron-transfer dynamics: rates, completeness and electronic coherence

The dynamics of electron injection from a donor state localized in the adsorbate into the semiconductor substrate can be simulated at the purely electronic level based on the analysis of the donor-state energy-distribution function $\rho_{\mathrm{d}}(\epsilon)$, as outlined in the computational methods section. Here, we present the time-evolution of population at the donor state for each system investigated and discuss the dynamical behavior. The major focus is on the rate of the ET process. Some other aspects of the heterogeneous ET reaction such as the incomplete character of ET and electronic coherence effects are also considered.

Electron injection from dye-S_1 to ZnO

Figure 12 shows the population of the donor state in all investigated systems after initial preparation at the dye-S_1 state by the instantaneous laser pulse. The decay of the donor-state population reflects the electron injection into the acceptor states in the ZnO substrate. The initial decay and the long-time dynamical behavior highly depend on the specific system. As one of the most interesting observables, the long-time rates of electron injection from the dye-S_1 donor state into the ZnO semiconductor, which are obtained by applying an exponential fit to the $P_{\mathrm{d}}(t)$ decay, are summarized in Table 1.

Interestingly, we have not observed any noticeable decay of the donor-state (dye-S_1) population for **1-a** within a simulation time of 2 ps; therefore it is not included in Figure 12(a). Since such a simulation time has already gone beyond the characteristic times of some other competing processes, for example, the charge recombination of the dye, our result indicates that no interfacial ET occurs from the dye-S_1 of the bound perylene-acrylic acid to the conduction band of a hydroxylated ZnO-(0001) surface. This finding reflects a negligible donor-acceptor coupling, which is a combined result of: (i) the very low density of isoenergetic acceptor states (*cf.* Figure 4(a)); and (ii) a very weak interaction between the donor state and the isoenergetic acceptor states, which is likely due to the large spatial separation between the donor-state and the acceptor-state charge-density distributions, as illustrated in Figure 5(b). Accordingly, the dye-LUMO energy distribution of **1-a** obtained from the GGA-DFT calculation exhibits a single peak with a typical δ-function character. Therefore the dye-LUMO is nearly an eigenstate of the one-particle Hamiltonian for the overall dye-semiconductor complex thus completely uncoupled to the acceptor space. Consequently, no transition dynamics occurs.

In contrast, for both **1-b** and **1-c** complexes we observe a significant decay of donor-state (dye-S_1) population. More specifically, Figure 12(a) shows a slower component in the first 60 fs for the dynamics in **1-b**, and a decay with a nearly monotonic exponential character for **1-c**. Therefore our results show that both defects — oxygen-vacancy at the topmost layer and zinc-interstitial at a deeper layer — favor electron injection from the excited state of the chemisorbed perylene-acrylic acid into the ZnO substrate. This can be rationalized as follows. For **1-b**, the oxygen-vacancy has effectively extended the charge density of dye-S_1 (which, as a molecular wire, has significant distribution over the spacer and anchor group) into the top ZnO-layers (*cf.* Figure 9(b)), thus strengthening the interaction with the isoenergetic acceptor states that are mainly distributed in deeper ZnO-layers. On the other hand, the zinc-interstitial introduces delocalized charge-density distribution over several ZnO-layers, thus effectively reducing the thickness of the "insulating layer" between the adsorbate and the bottom layers of ZnO (this can be clearly seen by comparing Figure 9(b) with Figure 11(b)).

Exponential fit for long-time dynamics results in a 310 fs characteristic time for the ET in **1-b**, while for **1-c** the characteristic time is 430 fs. ET times for both **1-b** and **1-c** indicate a slower ET when compared to the experimental result of 190 fs[52,56]. There are several possible sources for such a deviation, for example, our choice of a polar surface and the adsorption binding mode. Vibronic-coupling effects, neglected in the present study, might also be significant due to the very low density of isoenergetic acceptor states. The study of the importance of coupling to the vibrational motions is of interest for our future work.

For both **2-** and **2′**-ZnO systems, ET dynamics with all three considered surface models of ZnO reveal a number of interesting features (Figures 12(b) and (c)), which are quite different from those in the **1**-ZnO systems. First of all, the ET processes in both **2-** and **2′-a** are observed to occur on an ultrafast sub-picosecond timescale. More specifically, for **2-a**, there is a slow decay component in the first 100 fs which is followed by a nearly exponential decay with a characteristic time of 130 fs; for **2′**, the slow dynamics occurs in the first 120 fs and an exponential decay follows with a characteristic time of 160 fs. In both cases, noticeable oscillatory structures are superimposed on the decay in the initial stage, *i.e.*, the slow component of dynamics. This likely indicates electronic coherence, which could be further demonstrated by comparing to ET dynamics at the vibronic level.

The result that sub-picosecond electron injection is observed in both perylene-propionic acid adsorbed at the ZnO surface is very different to that in **1-a**. This finding agrees well with the electronic-structure results discussed previously: Figures 4(b) and (c) indicate a much higher density of isoenergetic acceptor states in **2-** and **2′-a** than **1-a**; Figures 5(e) and (h) show a significant extension of isoenergetic acceptor-state charge-density distribution into the ZnO-layers near the dye-semiconductor interfaces: both lead to a much stronger interaction between the dye-LUMO and the isoenergetic conduction-band states in **2-** and **2′-a** than in **1-a**, thus an ultrafast heterogeneous ET with some noticeable electronic coherence effects. The deviation between the characteristic ET times in **2-** and **2′-a** and the experimental result, 265 fs[52,56] can again be due to the choice of surface model and adsorption binding mode, as

well as the initial slow dynamics.

The influence of surface defects on the ET in both perylene-propionic acid / ZnO systems can be described based on Figures 12(b) and (c) as follows. In **2-b**, the removal of the oxygen near the adsorption center has rather weak impact on the ET: it causes a longer initial slow decay (for 120 fs), while the characteristic time of the following exponential decay is 130 fs identical to the result for **2-a**. The influence of oxygen-vacancy is slightly larger in **2′**: the slow dynamics remains for 120 fs, while the following decay has a characteristic time of 200 fs. In contrast, the zinc-interstitial in a deeper layer causes a slower ET with much less electronic coherence in both systems: the oscillatory structures can only be observed in the first 20 fs of dynamics, while globally the decay of donor-state population can be regarded as exponential. The characteristic times of ET in **2-** and **2′-c** are 190 fs and 500 fs, respectively.

The weak effect of oxygen-vacancy on the ET in **2-b** is expected to be related to the chemical nature of the saturated -CH_2CH_2- spacer group. Since the charge-density distribution in dye **2** is almost completely localized in the perylene chromophore, the rather localized charge-density around the oxygen-vacancy does not act as an extension of the molecular wire but rather, especially in **2′-b**, creates a repulsive interaction to the dye-LUMO charge-density due to the extra negative charge localized at the oxygen-vacancy site; this leads to a somewhat slower dynamics. Such a slower ET can also be observed in **2-c** and **2′-c**, where the extra electron of the interstitial zinc atom is substantially delocalized within the top ZnO-layers, thus reducing the probability of charge transfer. In particular, interfacial electron injection in **2′-c** is significantly slower than in **2′-a**, which can be rationalized by the large area of repulsive interaction between the donor-state (dye-LUMO) charge density distributed over the perylene chromophore and the negative charge delocalized within the top layers in ZnO.

Electron injection from dye-S_2 to ZnO

We are also interested in the electron injection from the dye-S_2 (represented by the dye-(LUMO+1)) to the ZnO semiconductor substrate. Such an ET process usually follows a 2-

photon excitation, which plays a nonnegligible role especially in some ZnO-based DSSCs[101]. Figure 13 shows the population of the donor state in all investigated systems after initial preparation at the dye-S_2 state by the instantaneous laser pulse. The rates of electron injection from the dye-S_2 donor state into the ZnO semiconductor are summarized in Table 2. Specifically, data for **1-b** and 1-c are obtained by applying the "$1/e$-time" concept, *i.e.*, the time when the donor-state population has decreased to $1/e$ or its initial value[97]; for the other four systems, ET rates listed in Table 2 are obtained by exponential fit and reflect long-time dynamics. The ultrafast charge transfer from a higher-energy charge transfer state is analogous to the situation seen in organic donor / acceptor interfaces. For instance[150], phthalocyanine (H_2Pc) / fullerene bilayer interfaces show that charge separation occurs from these hot states prior to relaxation to the lowest-energy CT exciton.

Significant effects from both defects, oxygen-vacancy and zinc-interstitial, can be observed in the perylene-acrylic acid (**1**) / ZnO systems (Figure 13(a)). In **1-a**, the decay of donor-state population is very smooth and nearly exponential with a characteristic time of 180 fs. In contrast, the much faster dynamics in both **1-b** and **1-c** are not exponential processes, and thus cannot be fully characterized by a single rate constant. These results reflect a stronger donor-acceptor coupling and, in particular, a much higher density of isoenergetic acceptor states in **1-b** and **1-c**. As a result, the decays of donor-state population in both defect-containing systems do not follow a purely exponential dynamics but rather exhibit some structures: an initial fast decay, a following slow component of dynamics, and a slower long-time dynamics. As an estimate of the overall characteristic ET times, we apply the "$1/e$-time" concept and obtain 30 fs for **1-b** and 40 fs for **1-c**. Both indicate a much faster electron injection from the dye-S_2 state than from the dye-S_1 state in the same systems.

The effects of surface defects on the ET rates (involving dye-S_2) are much smaller in the case of the dye with a saturated spacer. The time evolutions of the donor-state populations in **2-a**, **2-b** and **2-c** exhibit an initial slow component of dynamics and a following (nearly) exponential decay (Figure 13(b)). In particular, the initial slow dynamics in **2-a** lasts for 150 fs

and is much shorter in the other two systems (80 fs, and 50 fs for **2-b**, and **2-c**, respectively). The characteristic times of long-time ET in **2-a**, **2-b** and **2-c** are all about 150 fs. The effects on the ET rates in 2′-ZnO are somewhat larger: the characteristic long-time ET timescale in **2′-a**, **2′-b**, and **2′-c** are 220 fs, 110 fs, and 150 fs, respectively. It is especially worthwhile to notice that our results show that both types of vacancy favor a faster electron injection from dye-S_2 in **2′**-ZnO, which is very different from the trend in ET with dye-S_1 in **2′**-ZnO, as discussed above. In addition, Figures 13(b) and (c) exhibit significant electronic coherences on the early stage of dynamics, thus indicating a relatively strong electronic interaction between the donor and acceptor states. This is possibly a result of the significant increasing density of isoenergetic acceptor states.

Concluding remarks

We have studied a series of perylene-sensitized ZnO surfaces at the DFT level. The donor-acceptor interactions have been analyzed based on the calculated electronic properties, and the photoinduced electron-transfer processes from the dye into the ZnO surface have been simulated at the electronic level.

The results from the dynamical simulations show that the interfacial ET processes occur on an ultrafast (sub-picosecond) timescale in most of the investigated systems. ET rates and detailed dynamical behavior highly depend on the details of the electronic donor-acceptor interactions, which comes from a combination of the donor-acceptor coupling strength and the density of isoenergetic acceptor states. As a result of the rather low DOS near the CBM in ZnO, the latter factor plays a significant role in our study. In perylene-acrylic acid (unsaturated spacer) adsorbed on a fully hydroxylated ZnO-(111) surface, our simulations point to negligible photoinduced electron injection from the first excited state of the dye molecule to ZnO. This is due to the donor-level alignment at the CBM of ZnO, which corresponds to a very low density of isoenergetic acceptor states and very weak donor-acceptor coupling. In contrast,

a sub-picosecond ET timescale was obtained for perylene-propionic acid (saturated spacer) adsorbed on the fully hydroxylated ZnO-(111) surface.

Our results clearly show that both oxygen-vacancy and zinc-interstitial defects assist in the electron injection from the S_1 state of chemisorbed perylene-acrylic acid into the ZnO semiconductor. More specifically, the introduction of oxygen-vacancies leads to a faster long-time dynamics. In contrast, neither oxygen-vacancy nor zinc-interstitial results in a significantly faster ET in perylene-propionic acid / ZnO. In addition, both defects were shown to accelerate ET from the S_2 state of both dye molecules, more significantly for perylene-acrylic acid. Electron-density distribution calculations underline that the oxygen-vacancy can extend the electron density from the excited state of the dye molecule to the top ZnO-layer, while the zinc-interstitial creates a delocalized electron density over the second and third ZnO-layers. Both can significantly modify the donor-acceptor coupling schemes. The detailed mechanism of how these defects influence the ET dynamics is subject to future work. On the other hand, the influence of the surface defects on the ET rates in perylene-propionic acid sensitized systems is relatively smaller.

Our theoretical results agree reasonably well with the ET rates determined experimentally (within a factor of 2). However, they do not reproduce the relative trends for the different dye adsorbates. This finding motivates more detailed study on the considered systems, such as by choosing different ZnO surfaces and dye-ZnO binding modes, including further types of surface defects, as well as taking couplings to the vibrational motions into account. In addition, electronic-structure calculations at a higher level are expected to give a more accurate description of the donor-acceptor interactions that play a key role in the interfacial ET. We do believe, however, that the calculations reported here provide a relevant first step into the understanding of these complex systems.

Acknowledgments

This work was supported as part of the Center for Interface Science: Solar Electric Materials (CISSEM), an Energy Frontier Research Center funded by the U.S. Department of Energy, Office of Science, Basic Energy Sciences under Award Number DE-SC0001084 (JL, HL, PW, JLB). The computations reported here were performed at the Georgia Tech Center for Computational Molecular Science and Technology, funded through a NSF CRIF award (Grant No. CHE0946869) and by the Georgia Institute of Technology.

References

(1) Lu, W.; Lieber, C. M. Semiconductor nanowires. *J. Phys. D.: Appl. Phys.* **2006**, *39*, R387-R406.

(2) Peiró, A. M.; Ravirajan, P.; Govender, K.; Boyle, D. S.; O'Brien, P.; Bradley, D. D. C.; Nelson, J.; Durrant, J. R. Hybrid polymer/metal oxide solar cells based on ZnO columnar structures. *J. Mater. Chem.* **2006**, *16*, 2088-2096.

(3) Gonzales-Valls, I.; Lira-Cantu, M. Vertically-aligned nanostructures of ZnO for excitonic solar cells: A review. *Energy Environ. Sci.* **2009**, *2*, 19-34.

(4) Bolink, H. J.; Coronado, E.; Repetto, D.; Sessolo, M. Air stable hybrid organic-inorganic light emitting diodes using ZnO as the cathode. *Appl. Phys. Lett.* **2007**, *91*, 223501.

(5) Bolink, H. J.; Coronado, E.; Repetto, D.; Sessolo, M.; Barea, E. M.; Bisquet, J.; Garcia-Belmonte, G.; Prochazka, J.; Kavan, L. Inverted solution processable OLEDs using a metal oxide as an electron injection contact. *Adv. Funct. Mater.*, **2008**, *18*, 145-150.

(6) Bolink, H. J.; Coronado, E.; Orozco, J.; Sessolo, M. Efficient polymer light-emitting diode using air-stable metal oxides as electrodes. *Adv. Mater.* **2009**, *21*, 79-82.

(7) Bolink, H. J.; Coronado, E.; Sessolo, M. White hybrid organic-inorganic light-emitting diode using ZnO as the air-stable cathode. *Chem. Mater.* **2009**, *21*, 439-441.

(8) Bolink, H. J.; Brine, H.; Coronado, E.; Sessolo, M. Hybrid organic-inorganic light emitting diodes: Effect of the metal oxide. *J. Mater. Chem.* **2010**, *20*, 4047-4049.

(9) Bolink, H. J.; Brine, H.; Coronado, E.; Sessolo, M. Phosphorescent hybrid organic¨Cinorganic light-emitting diodes. *Adv. Mater.* **2010**, *22*, 2198-2201.

(10) Koster, L. J. A.; van Strien, W. J.; Beek, W. J. E.; Blom, P. W. M. Device operation of conjugated Polymer/zinc oxide bulk heterojunction solar cells. *Adv. Funct. Mater.* **2007**, *17*, 1297-1302.

(11) Lee, Y.-J.; Sounart, T. L.; Scrymgeour, D. A.; Voigt, J. A.; Hsu, J. W. P. Control of ZnO nanorod array alignment synthesized via seeded solution growth. *J. Cryst. Growth* **2007**, *304*, 80-85.

(12) Olson, D. C.; Lee, Y.-J.; White, M. S.; Kopidakis, N.; Shaheen, S. E.; Ginley, D. S.; Voigt, J. A.; Hsu, J. W. P. Effect of polymer processing on the performance of poly(3-hexylthiophene)/ZnO nanorod photovoltaic devices. *J. Phys. Chem. C* **2007**, *111*, 16640-16645.

(13) Olson, D. C.; Shaheen, S. E.; Collins, R. T.; Ginley, D. S. The effect of atmosphere and ZnO morphology on the performance of hybrid poly(3-hexylthiophene)/ZnO nanofiber photovoltaic devices. *J. Phys. Chem. C* **2007**, *111*, 16670-16678.

(14) Hau, S. K.; Yip. H.-L.; Baek, N. S.; Zou, J.; O'Malley, K.; Jen, A. K.-Y. Air-stable inverted flexible polymer solar cells using zinc oxide nanoparticles as an electron selective layer. *Appl. Phys. Lett.* **2008**, *92*, 253301.

(15) Monson, T. C.; Lloyd, M. T.; Olson, D. C.; Lee, Y.-J.; Hsu, J. W. P. Photocurrent enhancement in polythiophene- and alkanethiol-modified ZnO solar cells. *Adv. Mater.* **2008**, *20*, 4755-4759.

(16) Olson, D. C.; Lee, Y.-J.; White, M. S.; Kopidakis, N.; Shaheen, S. E.; Ginley, D. S.; Voigt, J. A.; Hsu, J. W. P. Effect of ZnO processing on the photovoltage of ZnO/poly(3-hexylthiophene) solar cells. *J. Phys. Chem. C* **2008**, *112*, 9544-9547.

(17) Liu, J. P.; Wang, S. S.; Bian, Z. Q.; Shan, M. N.; Huang, C. H. Inverted photovoltaic device based on ZnO and organic small molecule heterojunction. *Chem. Phys. Lett.* **2009**, *470*, 103-106.

(18) Lloyd, M. T.; Lee, Y.-J.; David, R. J.; Fang, E.; Fleming, R. M.; Hsu, J. W. P.; Kline, R. J.; Toney, M. F. Improved efficiency in poly(3-hexylthiophene)/zinc oxide solar cells via lithium incorporation. *J. Phys. Chem. C* **2009**, *113*, 17608-17612.

(19) Lloyd, M. T.; Prasankumar, R. P.; Sinclair, M. B.; Mayer, A. C.; Olson, D. C.; Hsu, J. W. P. Impact of interfacial polymer morphology on photoexcitation dynamics and device performance in P3HT/ZnO heterojunctions. *J. Mater. Chem.* **2009**, *19*, 4609-4614.

(20) Sekine, N.; Chou, C.-H.; Kwan, W. L.; Yang, Y. ZnO nano-ridge structure and its application in inverted polymer solar cell. *Org. Electron.* **2009**, *10*, 1473-1477.

(21) Spoerke, E. D.; Lloyd, M. T.; McCready, E. M.; Olson, D. C.; Lee, Y.-J.; Hsu, J. W. P. Improved performance of poly(3-hexylthiophene)/zinc oxide hybrid photovoltaics modified with interfacial nanocrystalline cadmium sulfide. *Appl. Phys. Lett.* **2009**, *95*, 213506.

(22) Uhlrich, J. J.; Olson, D. C.; Hsu, J. W. P.; Kuech, T. F. Surface chemistry and surface electronic properties of ZnO single crystals and nanorods. *J. Vac. Sci. Technol. A* **2009**, *27*, 328-335.

(23) Hsu, J. W. P.; Lloyd, M. T. Organic/inorganic hybrids for solar energy generation. *MRS Bull.* **2010**, *35*, 422-428.

(24) Yang, T.; Cai, W.; Qin, D.; Wang, E.; Lan, L.; Gong, X.; Peng, J.; Cao. Y. Solution-processed zinc oxide thin film as a buffer layer for polymer solar cells with an inverted device structure. *J. Phys. Chem. C* **2010**, *114*, 6849.

(25) Zhang, B.; Lee, D.-H.; Chae, H.-Y.; Park, C.-H.; Cho, S.-M. Optimization of inverted bulk heterojunction polymer solar cells. *Korean J. Chem. Eng.* **2010**, *27*, 999-1002.

(26) Cheun, H.-S.; Fuentes-Hernandez, C.; Zhou, Y.; Potscavage Jr., W. J.; Kim, S.-J.; Shim, J.-W.; Dindar, A.; Kippelen, B. Electrical and optical properties of ZnO processed by atomic layer deposition in inverted polymer solar cells. *J. Phys. Chem. C* **2010**, *114*, 20713-20718.

(27) Bailey, B. A.; Reese, M. O.; Olson, D. C.; Shaheen, S. E.; Kopidakis, N. Air-processed

organic photovoltaic devices fabricated with hot press lamination. *Org. Electron.* **2011**, *12*, 108-112.

(28) Keis, K.; Magnusson, E.; Lindström, H.; Lindquist, S.-E.; Hagfeldt, A. A 5% efficient photoelectrochemical solar cell based on nanostructured ZnO electrodes. *Sol. Energ. Mater. Sol. C.* **2002**, *73*, 51-58.

(29) Baxter, J. B.; Aydil, E. S. Nanowire-based dye-sensitized solar cells. *Appl. Phys. Lett.* **2005**, *86*, 053114.

(30) Law, M.; Greene, L. E.; Johnson, J. C.; Saykally, R.; Yang, P. Nanowire dye-sensitized solar cells. *Nat. Mater.* **2005**, *4*, 455-459.

(31) Galoppini, E.; Rochford, J.; Chen, H.; Saraf, G.; Lu, Y.; Hagfeldt, A.; Boschloo, G. Fast electron transport in metal organic vapor deposition grown dye-sensitized ZnO nanorod solar cells. *J. Phys. Chem. B* **2006**, *110*, 16159-16161.

(32) Memarian, N.; Concina, I; Braga, A.; Rozati, S. M.; Vomiero, A.; Sberveglieri, G. Hierarchically assembled ZnO nanocrystallites for high-efficiency dye-sensitized solar cells. *Angew. Chem.* **2011**, *123*, 12529-12533.

(33) O'Regan, B.; Grätzel, M. A low-cost, high-efficiency solar cell based on dye-sensitized colloidal TiO_2 films. *Nature* **1991**, *353*, 737-740.

(34) Hagfeldt, A.; Grätzel, M. Light-induced redox reactions in nanocrystalline systems. *Chem. Rev.* **1995**, *95*, 49-68.

(35) Wachtveitl, J.; Huber, R.; Spörlein, S.; Moser, J.-E.; Grätzel, M. Ultrafast photoinduced electron transfer in coumarin 343 sensitized TiO_2-colloidal solution. *Int. J. Photoenergy* **1999**, *1*, 153-155.

(36) Hagfeldt, A.; Grätzel, M. Molecular photovoltaics. *Acc. Chem. Res.* **2000**, *33*, 269-277.

(37) Asbury, J. B.; Hao, E.; Wang, Y.; Ghosh, H. N.; Lian, T. Ultrafast electron transfer dynamics from molecular adsorbates to semiconductor nanocrystalline thin films. *J. Phys. Chem. B* **2001**, *105*, 4545-4557.

(38) Grätzel, M. Photoelectrochemical cells. *Nature* **2001**, *414*, 338-344.

(39) Moser, J.-E.; Grätzel, M. Observation of temperature independent heterogeneous electron transfer reactions in the inverted Marcus region. *Chem. Phys.* **1993**, *176*, 493-500.

(40) Burfeindt, B.; Hannappel, T.; Storck, W.; Willig, F. Measurement of temperature-independent femtosecond interfacial electron transfer from an anchored molecular electron donor to a semiconductor as acceptor. *J. Phys. Chem.* **1996**, *100*, 16463-16465.

(41) Ghosh, H. N.; Asbury, J. B.; Weng, Y.; Lian, T. Interfacial Electron Transfer between $Fe(II)(CN)_6^{4-}$ and TiO_2 nanoparticles: Direct electron injection and nonexponential recombination. *J. Phys. Chem. B* **1998**, *102*, 10208-10215.

(42) Willig, F.; Zimmermann, C.; Ramakrishna S.; Storck, W. Ultrafast dynamics of light-induced electron injection from a molecular donor into the wide conduction band of a semiconductor as acceptor. *Electrochim. Acta* **2000**, *45*, 4565-4575.

(43) Zimmermann, C.; Willig, F.; Ramakrishna, S.; Burfeindt, B.; Pettinger, B.; Eichberger, R.; Storck, W. Experimental fingerprints of vibrational wave-packet motion during ultrafast heterogeneous electron transfer. *J. Phys. Chem. B* **2001**, *105*, 9245-9253.

(44) Kallioinen, J.; Benkö, G.; Sundström, V.; Korppi-Tommola, J. E. I.; Yartsev, A. P. Electron transfer from the singlet and triplet excited states of $Ru(dcbpy)_2(NCS)_2$ into nanocrystalline TiO_2 thin films. *J. Phys. Chem. B* **2002**, *106*, 4396-4404.

(45) Huber, R.; Moser, J.-E.; Grätzel, M.; Wachtveitl, J. Real-time observation of photoinduced adiabatic electron transfer in strongly coupled dye/semiconductor colloidal systems with a 6 fs time constant. *J. Phys. Chem. B* **2002**, *106*, 6494-6499.

(46) Schnadt, J.; Brühwiler, P. A.; Patthey, L.; O'Shea, J. N.; Södergren, S.; Odelius, M.; Ahuja, R.; Karis, O.; Bässler, M.; Persson, P. et al. Experimental evidence for sub-3-fs charge transfer from an aromatic adsorbate to a semiconductor. *Nature* **2002**, *418*, 620-623.

(47) Furube, A.; Katoh, R.; Hara, K.; Murata, S.; Arakawa, H.; Tachiya, M. Ultrafast stepwise electron injection from photoexcited Ru-complex into nanocrystalline ZnO film via intermediates at the surface. *J. Phys. Chem. B* **2003**, *107*, 4162-4166.

(48) Furube, A.; Katoh, R.; Yoshihara, T.; Hara, K.; Murata, S.; Arakawa, H.; Tachiya, M. Ultrafast direct and indirect electron-injection processes in a photoexcited dye-sensitized nanocrystalline zinc oxide film: The importance of exciplex intermediates at the surface. *J. Phys. Chem. B* **2004**, *108*, 12583-12592.

(49) Matylitsky, V. V.; Lenz, M. O.; Wachtveitl, J. Observation of pH-dependent back-electron-transfer dynamics in alizarin/TiO_2 adsorbates: Importance of trap states. *J. Phys. Chem. B* **2006**, *110*, 8372-8379.

(50) Ernstorfer, R.; Gundlach, G.; Felber, S.; Storck, W.; Eichberger, R.; Willig, F. Role of molecular anchor groups in molecule-to-semiconductor electron transfer. *J. Phys. Chem. B* **2006**, *110*, 25383-25391.

(51) Gundlach, L.; Ernstorfer, R.; Willig, F. Dynamics of photoinduced electron transfer from adsorbed molecules into solids. *Appl. Phys. A.* **2007**, *88*, 481-495.

(52) Szarko, J. M.; Neubauer, A.; Bartelt, A. F.; Socaciu-Siebert, L.; Birkner, F.; Schwarzburg, K.; Hannappel, T.; Eichberger, R. The ultrafast temporal and spectral characterization of electron injection from perylene derivatives into ZnO and TiO_2 colloidal films. *J. Phys. Chem. C.* **2008**, *112*, 10542.

(53) Dworak, L.; Matylitsky, V. V.; Wachtveitl, J. Ultrafast photoinduced processes in alizarin-sensitized metal oxide mesoporous films. *ChemPhysChem* **2009**, *10*, 384-391.

(54) Stockwell, D.; Yang, Y.; Huang, J.; Anfuso, C.; Huang, Z.; Lian, T. Comparison of electron-transfer dynamics from coumarin 343 to TiO_2, SnO_2, and ZnO nanocrystalline thin films: Role of interface-bound charge-separated pairs. *J. Phys. Chem. C* **2010**, *114*, 6560-6566.

(55) Němec, H.; Rochford, J.; Taratula, O.; Galoppini, E.; Kužel, P.; Polívka, T.; Yartsev. A. P.; Sundström, V. Influence of the electron-cation interaction on electron mobility in dye-sensitized ZnO and TiO_2 nanocrystals: A study using ultrafast terahertz spectroscopy. *Phys. Rev. Lett.* **2010**, *104*, 197401.

(56) Neubauer, A.; Szarko, J. M.; Bartelt, A. F.; Eichberger, R.; Hannappel, T. Photophysical study of perylene/TiO_2 and perylene/ZnO varying interfacial couplings and the chemical environment. *J. Phys. Chem. C* **2011**, *115*, 5683-5691.

(57) Rehm, J. M.; McLendon, G. L.; Nagasawa, Y.; Yoshihara, K.; Moser, J.-E.; Grätzel, M. Femtosecond electron-transfer dynamics at a sensitizing dye-semiconductor (TiO_2) interface. *J. Phys. Chem.* **1996**, *100*, 9577-9578.

(58) Benkö, G.; Kallioinen, J.; Korppi-Tommola, J. E. I.; Yartsev, A. P.; Sundström, V. Photoinduced ultrafast dye-to-semiconductor electron injection from nonthermalized and thermalized donor states. *J. Am. Chem. Soc.* **2002**, *124*, 489-493.

(59) Keis, K.; Lidgren, J.; Lindquist, S.-E.; Hagfeldt, A. Studies of the adsorption process of Ru complexes in nanoporous ZnO electrodes. *Langmuir* **2000**, *16*, 4688-4694.

(60) O'Regan, B.; Sklover, V.; Grätzel, M. Electrochemical deposition of smooth and homogeneously mesoporous ZnO films from propylene carbonate electrolytes. *J. Electrochem. Soc.* **2001**, *148*, C498-C505.

(61) Duncan, W. R.; Prezhdo, O. V. Theoretical studies of photoinduced electron transfer in dye-sensitized TiO_2. *Annu. Rev. Phys. Chem.* **2007**, *58*, 143-184.

(62) Kondov, I.; Vallet, V.; Wang, H.; Thoss, M. Ground- and excited-state properties of the mixed-valence complex $[(NH_3)_5Ru^{III}NCRu^{II}(CN)_5]^-$. *J. Phys. Chem. A* **2008**, *112*, 5467-5477.

(63) Prezhdo, O. V.; Duncan, W. R.; Prezhdo, V. V. Dynamics of the photoexcited electron at the chromophore¨Csemiconductor interface. *Acc. Chem. Res.* **2008**, *41*, 339-348.

(64) Martsinovich, N.; Troisi, A. Theoretical studies of dye-sensitised solar cells: From electronic structure to elementary processes. *Energy Environ. Sci.* **2011**, *4*, 4473-4495.

(65) Ramakrishna, S.; Willig, F. Pump-probe spectroscopy of ultrafast electron injection from the excited state of an anchored chromophore to a semiconductor surface in UHV: A theoretical model. *J. Phys. Chem. B* **2000**, *104*, 68-77.

(66) Ramakrishna, S.; Willig, F.; May, V. Photoinduced ultrafast electron injection from a surface attached molecule: Control of electronic and vibronic distributions via vibrational wave packets. *Phys. Rev. B* **2000**, *62*, R16330-R16333.

(67) Ramakrishna, S.; Willig, F.; May, V. Theory of ultrafast photoinduced heterogeneous electron transfer: Decay of vibrational coherence into a finite electronic¨Cvibrational quasicontinuum. *J. Chem. Phys.* **2001**, *115*, 2743-2756.

(68) Ramakrishna, S.; Willig, F.; May, V. Bridge mediated ultrafast heterogeneous electron transfer. *Chem. Phys. Lett.* **2002**, *351*, 242-250.

(69) Ramakrishna, S.; Willig, F.; May, V.; Knorr, A. Femtosecond spectroscopy of heterogeneous electron transfer: Extraction of excited-state population dynamics from pump-probe signals. *J. Phys. Chem. B* **2003**, *107*, 607-611.

(70) Wang, L.; May, V. Laser pulse control of ultrafast heterogeneous electron transfer: A computational study. *J. Chem. Phys.* **2004**, *121*, 8039-8049.

(71) Wang, L.; Ernstorfer, R.; Willig, F.; May, V. Absorption spectra related to heterogeneous electron transfer reactions: The perylene TiO_2 system. *J. Phys. Chem. B* **2005**, *109*, 9589-9595.

(72) Wang, L.; Willig, F.; May, V. Ultrafast heterogeneous electron transfer reactions: Comparative theoretical studies on time- and frequency-domain data. *J. Chem. Phys.* **2006**, *124*, 014712.

(73) Petersson, Å.; Ratner, M. A.; Karlsson, H. O. Injection time in the metaloxide-molecule interface calculated within the tight-binding model. *J. Phys. Chem. B* **2000**, *104*, 8498-8502.

(74) Persson, P.; Bergström, R.; Lunell, S. Quantum chemical study of photoinjection processes in dye-sensitized TiO_2 nanoparticles. *J. Phys. Chem. B* **2000**, *104*, 10348-10351.

(75) Persson, P.; Lunell, S.; Ojamäe, L. Electronic interactions between aromatic adsorbates and metal oxide substrates calculated from first principles. *Chem. Phys. Lett.* **2002**, *364*, 469-474.

(76) Persson, P.; Bergström, R.; Ojamäe, L.; Lunell, S. Quantum-chemical studies of metal oxides for photoelectrochemical applications. *Adv. Quant. Chem.* **2002**, *41*, 203-263.

(77) Persson, P.; Lundqvist, M. J. Calculated structural and electronic interactions of the ruthenium dye N3 with a titanium dioxide nanocrystal. *J. Phys. Chem. B* **2005**, *109*, 11918-11924.

(78) Nilsing, M.; Persson, P.; Ojamäe, L. Anchor group influence on molecule¨Cmetal oxide interfaces: Periodic hybrid DFT study of pyridine bound to TiO_2 via carboxylic and phosphonic acid. *Chem. Phys. Lett.* **2005**, *415*, 375-380.

(79) Lundqvist, M. J.; Nilsing, M.; Persson, P.; Lunell, S. DFT study of bare and dye-sensitized TiO_2 clusters and nanocrystals. *Int. J. Quant. Chem.* **2006**, *106*, 3214-3234.

(80) Persson, P.; Lundqvist, M. J.; Ernstorfer, R.; Goddard III, W. A.; Willig, F. Quantum chemical calculations of the influence of anchor-cum-spacer groups on femtosecond electron transfer times in dye-sensitized semiconductor nanocrystals. *J. Chem. Theory Comput.* **2006**, *2*, 441-451.

(81) Schreiber, M.; Kondov, I.; Kleinekathöfer, U. A density matrix approach to photoinduced electron injection. *J. Lumin.* **2001**, *94*, 471-474.

(82) Stier, W. M.; Prezhdo, O. V. Nonadiabatic molecular dynamics simulation of light-induced electron transfer from an anchored molecular electron donor to a semiconductor acceptor. *J. Phys. Chem. B* **2002**, *106*, 8047-8054.

(83) Stier, W. M.; Prezhdo, O. V. Thermal effects in the ultrafast photoinduced electron transfer from a molecular donor anchored to a semiconductor acceptor. *Israel J. Chem.* **2002**, *42*, 213-224.

(84) Stier, W. M.; Duncan, W. R.; Prezhdo, O. V. Thermally assisted sub-10 fs electron transfer in dye-sensitized nanocrystalline TiO_2 solar cells. *Adv. Mater.* **2004**, *16*, 240-244.

(85) Duncan, W. R.; Prezhdo, O. V. Electronic structure and spectra of catechol and alizarin in the gas phase and attached to titanium. *J. Phys. Chem. B* **2005**, *109*, 365-373.

(86) Duncan, W. R.; Stier, W. M.; Prezhdo, O. V. *Ab initio* nonadiabatic molecular dynamics of the ultrafast electron injection across the alizarin-TiO_2 interface. *J. Am. Chem. Soc.* **2005**, *127*, 7941-7951.

(87) Duncan, W. R.; Prezhdo, O. V. Nonadiabatic molecular dynamics study of electron transfer from alizarin to the hydrated Ti^{4+} ion. *J. Phys. Chem. B* **2005**, *109*, 17998-18002.

(88) Rego, L. G. C.; Batista, V. S. Quantum dynamics simulations of interfacial electron transfer in sensitized TiO_2 semiconductors. *J. Am. Chem. Soc.* **2003**, *125*, 7989-7997.

(89) Rego, L. G. C.; Abuabara, S. G.; Batista, V. S. Model study of coherent quantum dynamics of hole states in functionalized semiconductor nanostructures. *J. Chem. Phys.* **2005**, *122*, 154709.

(90) Abuabara, S. G.; Rego, L. G. C.; Batista, V. S. Influence of thermal fluctuations on interfacial electron transfer in functionalized TiO_2 semiconductors. *J. Am. Chem. Soc.* **2005**, *127*, 18234-18242.

(91) Thoss, M.; Kondov, I.; Wang, H. Theoretical study of ultrafast heterogeneous electron transfer reactions at dye¨Csemiconductor interfaces. *Chem. Phys.* **2004**, *304*, 169-181.

(92) Kondov, I.; Thoss, M.; Wang, H. Theoretical study of ultrafast heterogeneous electron transfer reactions at dye-semiconductor interfaces: Coumarin 343 at titanium oxide. *J. Phys. Chem. A* **2006**, *110*, 1364-1374.

(93) Kondov, I.; Wang, H.; Thoss, M. Computational study of titanium (IV) complexes with organic chromophores. *Int. J. Quant. Chem.* **2006**, *106*, 1291-1303.

(94) Sebastian, K. L.; Tachiya, M. Theory of photoinduced heterogeneous electron transfer. *J. Chem. Phys.* **2006**, *124*, 064713.

(95) Liang, K. K.; Lin, C.-K.; Chang, H.-C.; Hayashi, M.; Lin, S. H. Theoretical treatments of ultrafast electron transfer from adsorbed dye molecule to semiconductor nanocrystalline surface. *J. Chem. Phys.* **2006**, *125*, 154706.

(96) Kondov, I.; Čížek, M.; Benesch, C.; Wang, H.; Thoss, M. Quantum dynamics of photoinduced electron-transfer reactions in dye-semiconductor systems: First-principles description and application to coumarin 343-TiO_2. *J. Phys. Chem. C* **2007**, *111*, 11970-11981.

(97) Li, J; Nilsing, M.; Kondov, I.; Wang, H.; Persson, P.; Lunell, S.; Thoss, M. Dynamical simulation of photoinduced electron transfer reactions in dye-semiconductor systems with different anchor groups. *J. Phys. Chem. C* **2008**, *112*, 12326-12333.

(98) Li, J.; Kondov, I.; Wang, H.; Thoss, M. Theoretical study of photoinduced electron-transfer processes in the dye-semiconductor system alizarin-TiO_2. *J. Phys. Chem. C* **2010**, *114*, 18481-18493.

(99) Li, J.; Wang, H.; Persson, P.; Thoss, M. Photoinduced electron transfer processes in dye-semiconductor systems with different spacer groups. *J. Chem. Phys.* **2012**, *137*, 22A529.

(100) Li, J.; Kondov, I.; Wang, H.; Thoss, M. Quantum dynamical simulation of photoinduced electron transfer processes in dye-semiconductor systems: Theory and application to coumarin 343 at TiO_2. *J. Phys.: Condens. Matter* **2015**, *27*, 134202.

(101) Labat, F.; Ciofini, I.; Hratchian, H. P.; Frisch, M.; Raghavachari, K.; Adamo, C. First principles modeling of eosin-loaded ZnO films: A step toward the understanding of dye-sensitized solar cell performances. *J. Am. Chem. Soc.* **2009**, *131*, 14290-14298.

(102) Ambrosio, F.; Martsinovich, N.; Troisi, A. Effect of the anchoring group on electron injection: Theoretical study of phosphonated dyes for dye-sensitized solar cells. *J. Phys. Chem. C* **2012**, *116*, 2622-2629.

(103) Syzgantseva, O. A.; Puska, M.; Laasonen, K. Physical factors affecting charge transfer at the Pe-COOH-TiO_2 anatase interface. *J. Phys. Chem. C* **2014**, *118*, 25310-25319.

(104) Amat, A.; de Angelis, F. Challenges in the simulation of dye-sensitized ZnO solar cells: Quantum confinement, alignment of energy levels and excited state nature at the dye/semiconductor interface. *Phys. Chem. Chem. Phys.* **2012**, *14*, 10662-10668.

(105) Vittadini, A.; Selloni, A.; Rotzinger, F. P.; Grätzel, M. Formic acid adsorption on dry and hydrated TiO_2 anatase (101) surfaces by DFT calculations. *J. Phys. Chem. B* **2000**, *104*, 1300-1306.

(106) Martsinovich, N.; Troisi, A. High-throughput computational screening of chromophores for dye-sensitized solar cells. *J. Phys. Chem. C* **2011**, *115*, 11781-11792.

(107) Mosconi, E.; Selloni, A.; de Angelis, F. Solvent effects on the adsorption geometry and electronic structure of dye-sensitized TiO_2: A first-principles investigation. *J. Phys. Chem. C* **2012**, *116*, 5932-5940.

(108) Prezhdo, O. V.;Duncan, W. R.; Prezhdo, V. V. Photoinduced electron dynamics at the chromophore¨Csemiconductor interface: A time-domain *ab initio* perspective. *Prog. Surf. Sci.* **2009**, *84*, 30-68.

(109) Tully, J. C. Molecular dynamics with electronic transitions. *J. Chem. Phys.* **1990**, *93*, 1061-1071.

(110) Craig, C. F.; Duncan, W. R.; Prezhdo, O. V. Trajectory surface hopping in the time-dependent Kohn-Sham approach for electron-nuclear dynamics. *Phys. Rev. Lett.* **2005**, *95*, 163001.

(111) Madelung, O. *Semiconductors: Data Handbook*; 3rd Ed. Springer: Berlin, 2004; pp 194-200.

(112) Li, H.; Schirra, L. K.; Shim, J.-W.; Cheun, H.-S.; Kippelen, B.; Monti, O. L. A.; Brédas, J.-L. Zinc oxide as a model transparent conducting oxide: A theoretical and experimental study of the impact of hydroxylation, vacancies, interstitials, and extrinsic doping on the electronic properties of the polar ZnO (0002) surface. *Chem. Mater.* **2012**, *24*, 3044-3055.

(113) Look, D. C.; Hemsky, J. W.; Sizelove, J. R. Residual native shallow donor in ZnO. *Phys. Rev. Lett.* **1999**, *82*, 2552-2555.

(114) Lavrov, E. V.; Weber, J.; Börrnert, F.; van de Walle, C. G.; Helbig, R. Hydrogen-related defects in ZnO studied by infrared absorption spectroscopy. *Phys. Rev. B* **2002**, *66*, 165205.

(115) Tuomisto, F.; Ranki, V.; Saarinen, K.; Look, D. C. Evidence of the Zn vacancy acting as the dominant acceptor in n-type ZnO. *Phys. Rev. Lett.* **2003**, *91*, 205502.

(116) Tuomisto, F.; Saarinen, K.; Look, D. C.; Farlow, G. C. Introduction and recovery of point defects in electron-irradiated ZnO. *Phys. Rev. B* **2005**, *72*, 085206.

(117) Özgür, Ü; Alivov, Y. I.; Liu, C.; Teke, A.; Reshchikov, M. A.; Doğan, S.; Avrutin, V.; Cho, S.-J.; Morkoç, H. A comprehensive review of ZnO materials and devices. *J. Appl. Phys.* **2005**, *98*, 041301.

(118) Kohan, A. F.; Ceder, G.; Morgan, D.; van de Walle, C. G. First-principles study of native point defects in ZnO. *Phys. Rev. B* **2000**, *61*, 15019-15027.

(119) Van de Walle, C. G. Hydrogen as a cause of doping in zinc oxide. *Phys. Rev. Lett.* **2000**, *85*, 1012-1015.

(120) Zhang, S.; Wei, S.; Zunger, A. Intrinsic n-type versus p-type doping asymmetry and the defect physics of ZnO. *Phys. Rev. B* **2001**, *63*, 075205.

(121) Janotti, A.; van de Walle, C. G. Oxygen vacancies in ZnO. *Appl. Phys. Lett.* **2005**, *87*, 122102.

(122) Janotti, A.; van de Walle, C. G. Native point defects in ZnO. *Phys. Rev. B* **2007**, *76*, 165202.

(123) Janotti, A.; van de Walle, C. G. Fundamentals of zinc oxide as a semiconductor. *Rep. Prog. Phys.* **2009**, *72*, 126501.

(124) Lany, S.; Zunger, A. Anion vacancies as a source of persistent photoconductivity in II-VI and chalcopyrite semiconductors. *Phys. Rev. B* **2005**, *72*, 035215.

(125) Lany, S.; Zunger, A. Dopability, intrinsic conductivity, and nonstoichiometry of transparent conducting oxides. *Phys. Rev. Lett.* **2007**, *98*, 045501.

(126) Lany, S.; Zunger, A. Many-body *GW* calculation of the oxygen vacancy in ZnO. *Phys. Rev. B* **2010**, *81*, 113201.

(127) De Angelis, F.; Armelao, L. Optical properties of ZnO nanostructures: A hybrid DFT/TDDFT investigation. *Phys. Chem. Chem. Phys.* **2011**, *13*, 467-475.

(128) Kisi, E. H.; Elcombe, M. M. u parameters for the wurtzite structure of ZnS and ZnO using powder neutron diffraction. *Acta Cryst.* **1989**, *C45*, 1867-1870.

(129) Neugenbauer, J.; Scheffler, M. Adsorbate-substrate and adsorbate-adsorbate interactions of Na and K adlayers on Al(111). *Phys. Rev. B* **1992**, *46*, 16067-16080.

(130) Kresse, G.; Hafner, J. *Ab initio* molecular-dynamics simulation of the liquid-metal-amorphous-semiconductor transition in germanium. *Phys. Rev. B* **1994**, *49*, 14251-14269.

(131) Kresse, G.; Furthmüller, J. Efficiency of *ab-initio* total energy calculations for metals and semiconductors using a plane-wave basis set. *Comput. Mater. Sci.* **1996**, *6*, 15-50.

(132) Kresse, G.; Furthmüller, J. Efficient iterative schemes for *ab initio* total-energy calculations using a plane-wave basis set. *Phys. Rev. B* **1996**, *54*, 11169-11186.

(133) Perdew, J. P.; Burke, K.; Ernzerhof, K. Generalized gradient approximation made simple. *Phys. Rev. Lett.* **1996**, *77*, 3865-3868.

(134) Blöchl, P. E. Projector augmented-wave method. *Phys. Rev. B* **1994**, *50*, 17953-17979.

(135) Dudarev, S. L.; Botton, G. A.; Savrasov, S. Y.; Humphreys, C. J.; Sutton, A. P. Electron-energy-loss spectra and the structural stability of nickel oxide: An LSDA+U study. *Phys. Rev. B* **1998**, *57*, 1505-1509.

(136) Palacios, P.; Sánchez, K.; Wahnón, P. *Ab-initio* valence band spectra of Al, In doped ZnO. *Thin Solid Films* **2009**, *517*, 2448-2451.

(137) Powell, R. A.; Spicer W. E.; McMenanmin, J. C. Location of the Zn 3d states in ZnO. *Phys. Rev. Lett.* **1971**, *27*, 97-100.

(138) Newns, D. M. Self-consistent model of hydrogen chemisorption. *Phys. Rev.* **1969**, *178*, 1123-1135.

(139) Sebastian, K. L. Electrochemical electron transfer: Accounting for electron-hole excitations in the metal electrode. *J. Chem. Phys.* **1989**, *90*, 5056-5067.

(140) See, *e.g.*, Beck, M. H.; Jäckle, A.; Worth, G. A.; Meyer, H.-D. The multicon"guration time-dependent Hartree (MCTDH) method: A highly effcient algorithm for propagating wavepackets. *Phys. Rep.* **2000**, *324*, 1-105.

(141) Wang, H.; Thoss, M. Multilayer formulation of the multiconfiguration time-dependent Hartree theory. *J. Chem. Phys.* **2003**, *119*, 1289-1299.

(142) Wang, H.; Thoss, M. Quantum-mechanical evaluation of the Boltzmann operator in correlation functions for large molecular systems: A multilayer multiconfiguration time-dependent Hartree approach. *J. Chem. Phys.* **2006**, *124*, 034114.

(143) See, *e.g.*, Tannor, D. J. *Introduction to Quantum Mechanics: A Time-Dependent Perspective*; University Science Press: Sausalito, 2007.

(144) Walsh, A.; da Silva, J. L. F.; Yan, Y.; Al-Jassim, M. M.; Wei, S.-H. Origin of electronic and optical trends in ternary $In_2O_3(ZnO)_n$ transparent conducting oxides ($n = 1, 3, 5$): Hybrid density functional theory calculations. *Phys. Rev. B* **2009**, *79*, 073105.

(145) Azpiroz, J. M.; Mosconi, E.; de Angelis, F. Modeling ZnS and ZnO nanostructures: Structural, electronic, and optical properties. *J. Phys. Chem. C* **2011**, *115*, 25219-25226.

(146) Flores, F.; Ortega, J.; Vázquez, H. Modelling energy level alignment at organic interfaces and density functional theory. *Phys. Chem. Chem. Phys.* **2009**, *11*, 8658-8675.

(147) Freysoldt, C.; Rinke, P.; Scheffler, M. Controlling polarization at insulating surfaces: Quasiparticle calculations for molecules adsorbed on insulator films. *Phys. Rev. Lett.* **2009**, *103*, 056803.

(148) Garcia-Lastra, J. M.; Rostgaard, C.; Rubio, A.; Thygesen, K. S. Polarization-induced renormalization of molecular levels at metallic and semiconducting surfaces. *Phys. Rev. B* **2009**, *80*, 245427.

(149) Aryasetiawan, F.; Gunnarson, O. The *GW* method. *Rep. Prog. Phys.* **1998**, *61*, 237-312.

(150) Jailaubekov, A. E.; Willard, A. P.; Tritsch, J. R.; Chan, W.-L.; Sai, N.; Gearba, R.; Kaake, L. G.; Williams, K. J.; Leung, K.; Rossky, P. J. et al. Hot charge-transfer excitons set the time limit for charge separation at donor/acceptor interfaces in organic photovoltaics. *Nature Mater.* **2013**, *12*, 66-73.

Tables and Figures

Table 1: Characteristic times (long-time dynamics) of electron injection from the dye-S_1 donor state to the ZnO conduction band for all investigated systems. All data are given in fs.

surface model	dye adsorbate **1**	**2**	**2′**
a	–	130	160
b	310	130	200
c	430	190	500

Table 2: Characteristic times ($1/$e-time for 1-b and 1-c; long-time dynamics in the other systems) of electron injection from the dye-S_2 donor state to the ZnO conduction band for all investigated systems. All data are given in fs.

surface model	dye adsorbate **1**	**2**	**2′**
a	180	150	220
b	30	74	110
c	40	150	150

Figure 1: Chemical structures of the perylene dyes investigated: Pe-CH=CH-COOH-ZnO (**1**) and Pe-CH_2CH_2-COOH-ZnO (**2**).

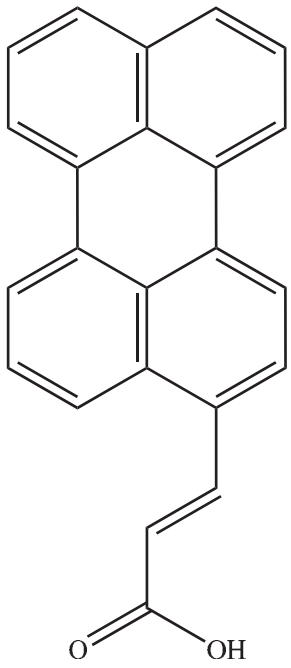

1

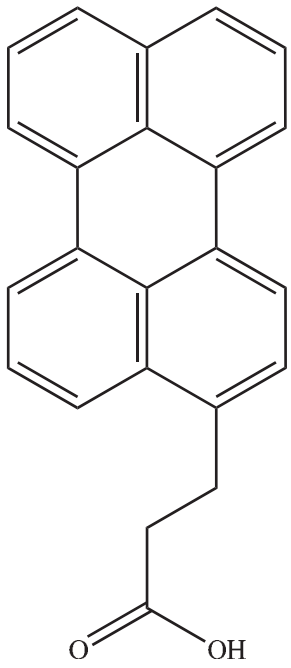

2

Figure 2: The three complexes with a hydroxylated ZnO surface considered in this paper: Pe-CH=CH-COOH-ZnO (**1-a**), Pe-CH_2CH_2-COOH-ZnO with a nearly perpendicular adsorption geometry (**2-a**) and Pe-CH_2CH_2-COOH-ZnO with a nearly parallel adsorption geometry (**2′-a**). Shown are relaxed structures within one unit cell in the slabs. The carbon, oxygen, zinc and hydrogen atoms are represented by the green, red, dark cyan and light gray spheres, respectively. A side view of **2′-a** is given from a different direction for a better illustration of the adsorption geometry.

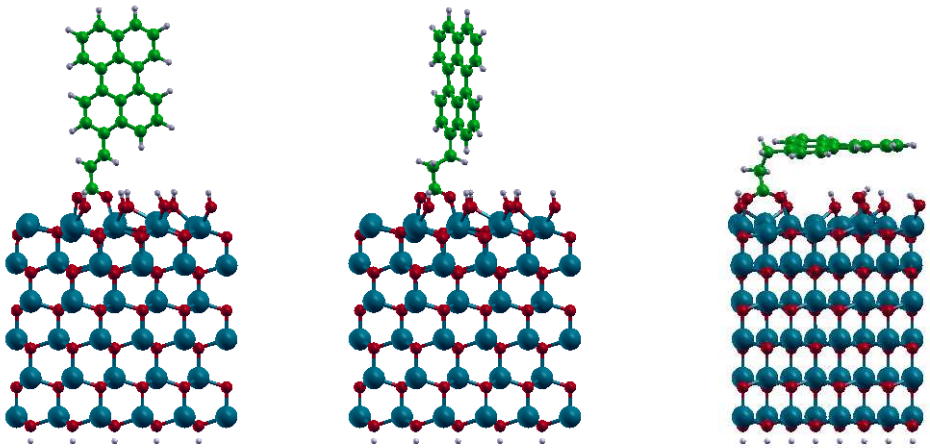

1-a **2-a** **2′-a**

Figure 3: The six complexes with a vacancy-containing ZnO surface considered in the present study: Pe-CH=CH-COOH-ZnO_{1-x} (**1-b**), Pe-CH_2CH_2-COOH-ZnO_{1-x} with a nearly perpendicular adsorption geometry (**2-b**), Pe-CH_2CH_2-COOH-ZnO_{1-x} with a nearly parallel adsorption geometry (**2′-b**), Pe-CH=CH-COOH-$Zn_{1+x}O$ (**1-c**), Pe-CH_2CH_2-COOH-$Zn_{1+x}O$ with a nearly perpendicular adsorption geometry (**2-c**) and Pe-CH_2CH_2-COOH-$Zn_{1+x}O$ with a nearly parallel adsorption geometry (**2′-c**). Shown are relaxed structures within one unit cell in the slabs. The positions of the removed oxygens are indicated by the red arrows in **1-b**, **2-b** and **2′-b**; the inserted zinc atoms are shown in **1-c**, **2-c** and **2′-c**. Side views are given from different directions for a better illustration of the adsorption geometries and the oxygen-vacancy positions.

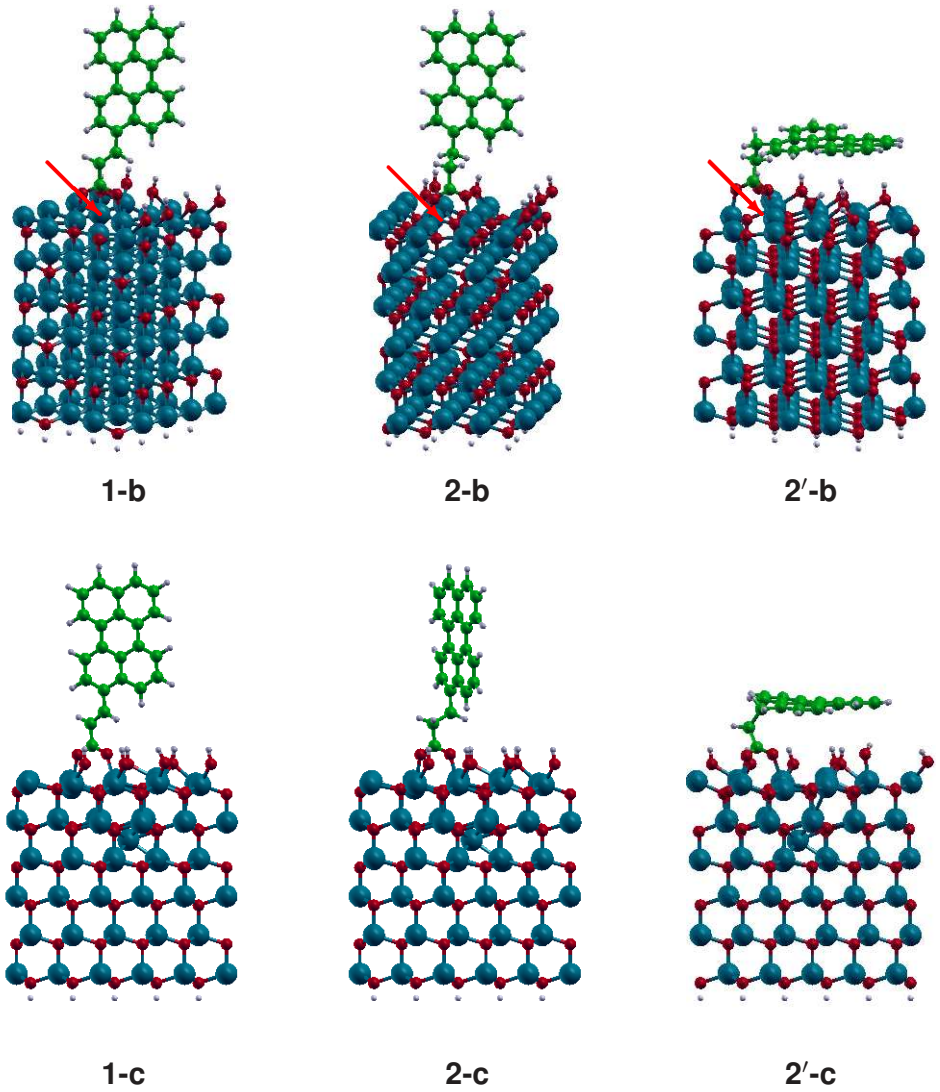

Figure 4: Partial-density-of-state (PDOS) schemes of the investigated complexes: (a) **1**, (b) **2** and (c) **2′** adsorbed on a hydroxylated zinc-terminated ZnO-(0001) surfaces (model **a**) as well as (d) the corresponding bare ZnO surface. Shown are the PDOS projected onto the dye adsorbates (black lines), the valence orbitals of oxygen atoms in the semiconductor substrate (red lines), the 3d orbitals of zinc atoms (green lines), and the 4s orbitals of zinc atoms (blue lines). Peaks in dye-PDOS schemes that correspond to the dye-HOMO, dye-LUMO and dye-(LUMO+1) levels are indicated. All PDOS are shown as functions of energy with respect to the VBM.

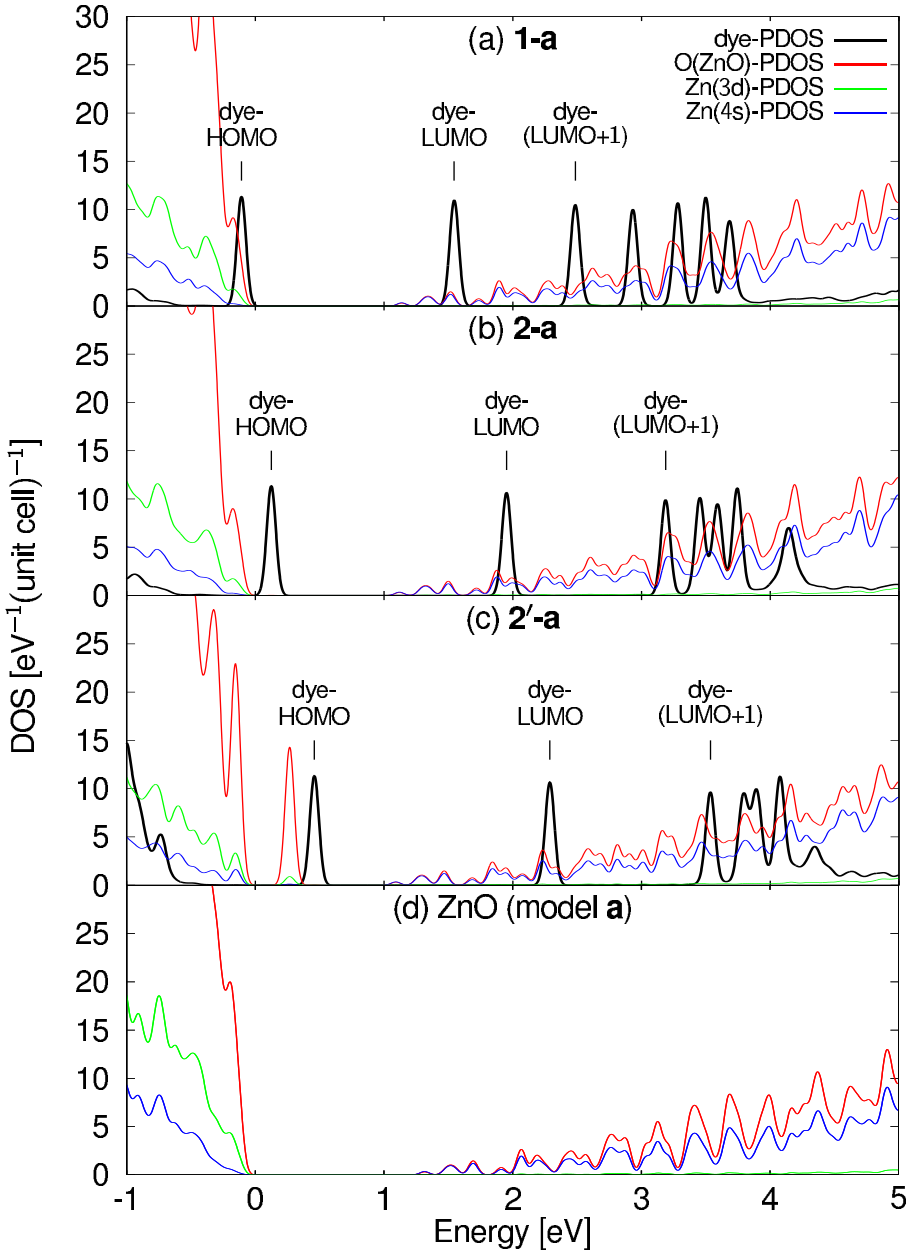

Figure 5: Charge-density distribution of the investigated systems: (a-c) **1-a**, (d-f) **2-a** and (g-i) **2′-a**. Shown are charge densities around (a, d, g) the dye-HOMO level, (b, e, h) the dye-LUMO level and (c, f, i) the dye-(LUMO+1) level.

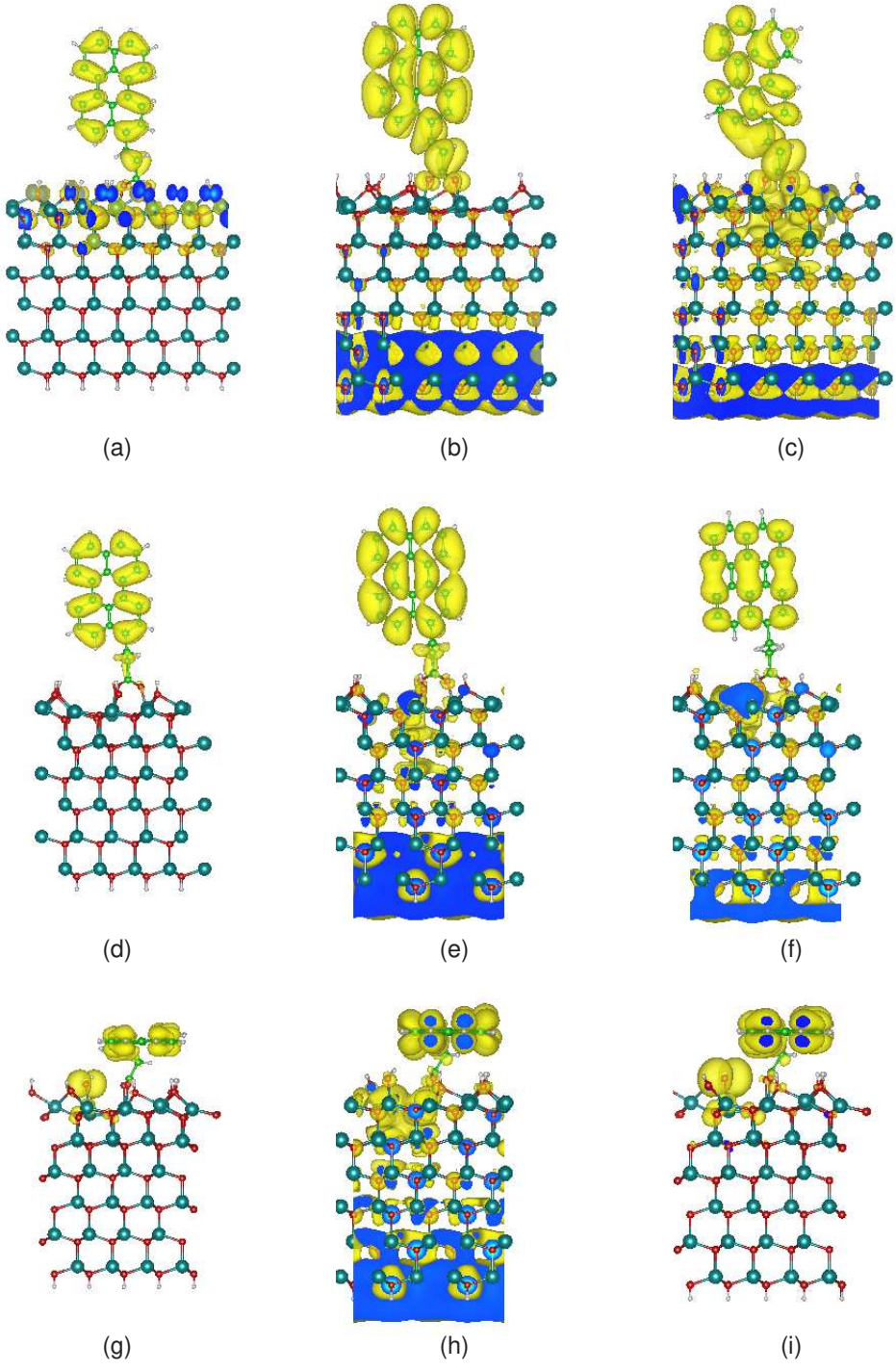

Figure 6: PDOS schemes of the investigated complexes: (a) **1**, (b) **2** and (c) **2′** adsorbed on an oxygen-vacancy containing zinc-terminated ZnO-(0001) surfaces (model **b**) as well as (d) the corresponding bare ZnO surface. The legends in Figure 4 are adopted. The PDOS peaks introduced by the oxygen-vacancy and the Fermi levels (E_F) are indicated by $*$ and vertical dashed lines, respectively. All PDOS are shown as a function of energy *vs.* the VBM.

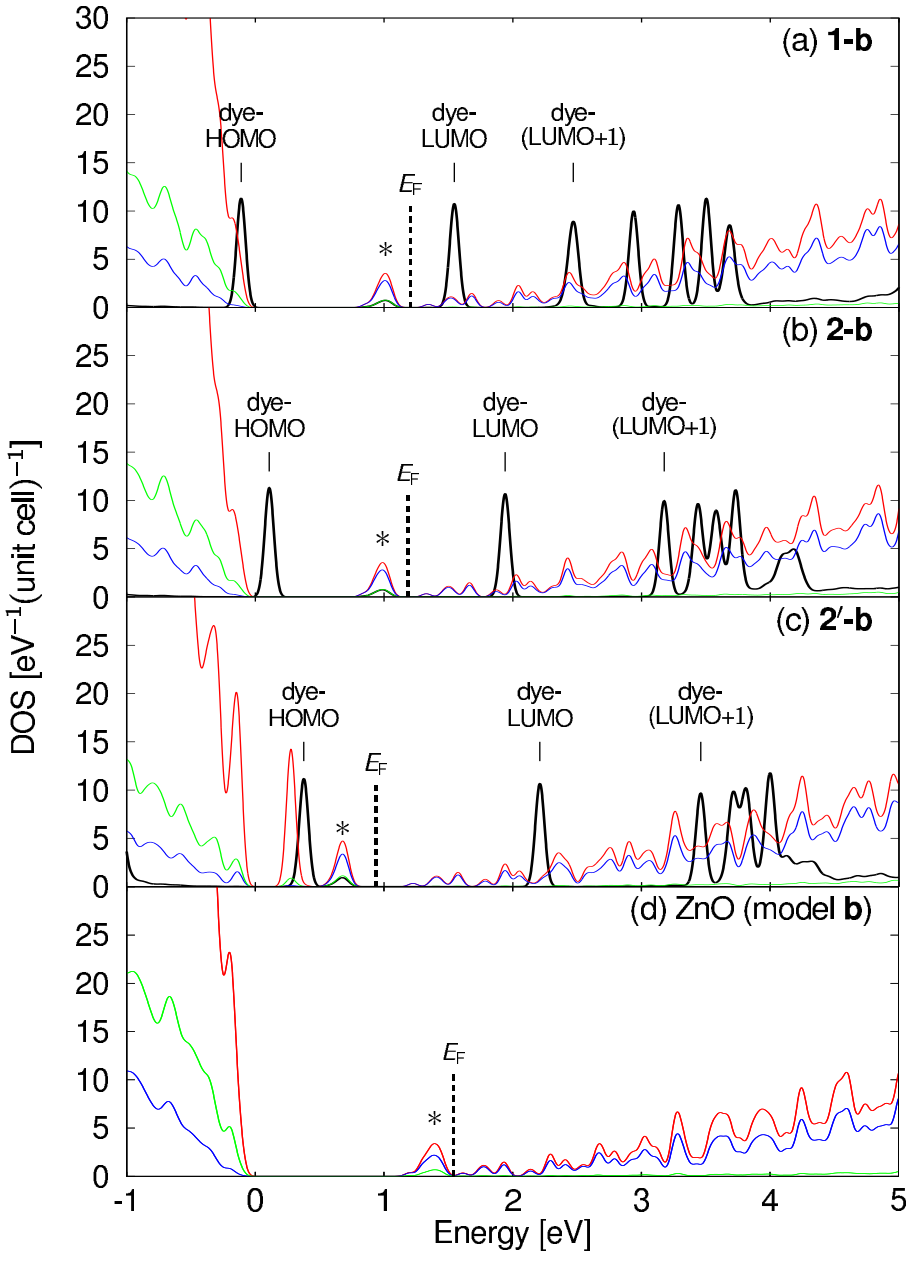

Figure 7: PDOS schemes of the investigated complexes: (a) **1**, (b) **2** and (c) **2′** adsorbed at an zinc-interstitial containing zinc-terminated ZnO-(0001) surfaces (model **c**) as well as (d) the corresponding bare ZnO surface. The legends in Figure 4 are adopted. Fermi levels (E_F) are indicated by $*$ and vertical dashed lines. All PDOS are shown as a function of energy *vs.* VBM.

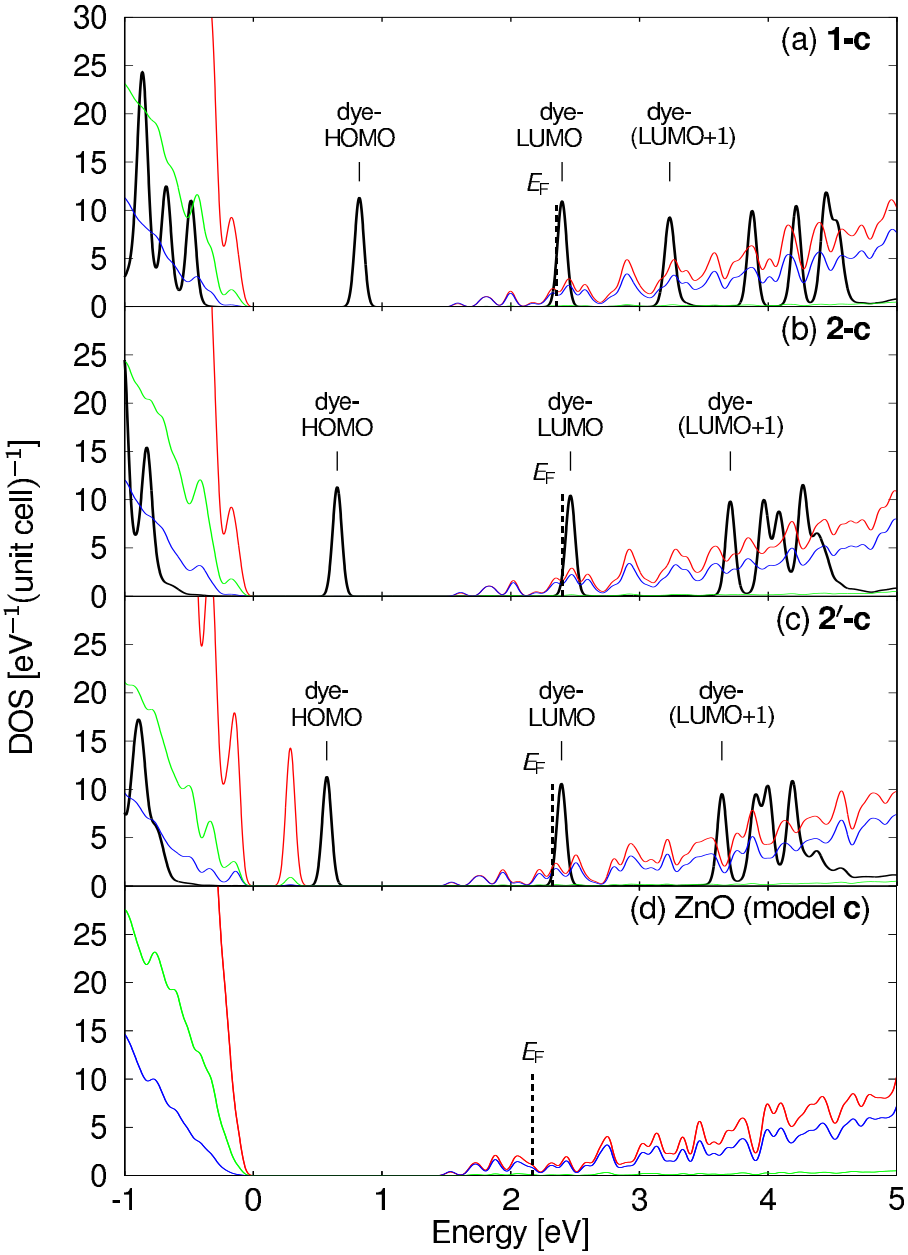

Figure 8: Charge-density distribution of the “oxygen-vacancy state” of the investigated systems with an oxygen-vacancy containing ZnO surface: (a) **1-b**, (b) **2-b**, and (c) **2′-b**.

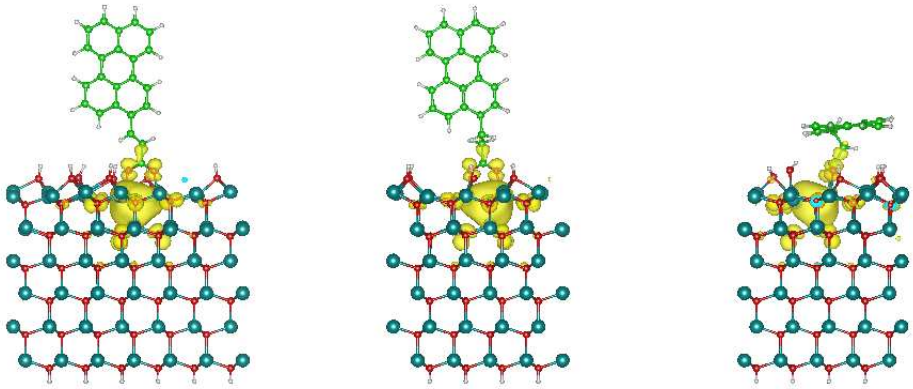

(a) (b) (c)

Figure 9: Charge-density distribution of the investigated systems with an oxygen-vacancy containing ZnO surface: (a-c) **1-b**, (d-f) **2-b** and (g-i) **2′-b**. Shown are charge densities around (a, d, g) the dye-HOMO level, (b, e, h) the dye-LUMO level and (c, f, i) the dye-(LUMO+1) level.

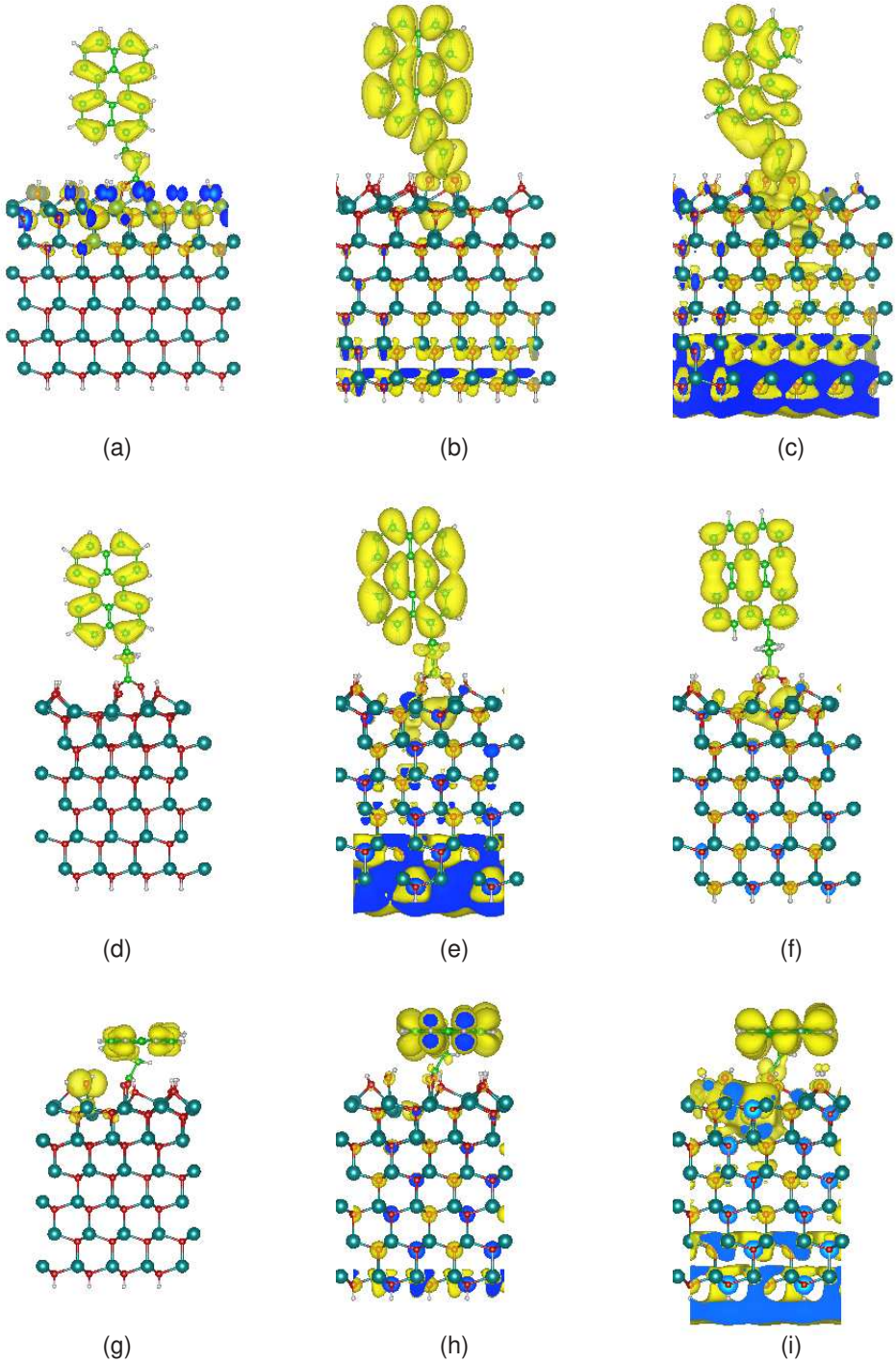

Figure 10: Charge-density distribution of conduction-band states at the bottom of the conduction band of the investigated systems with a zinc-interstitial containing ZnO surface: (a) **1-c**, (b) **2-c**, and (c) **2′-c**.

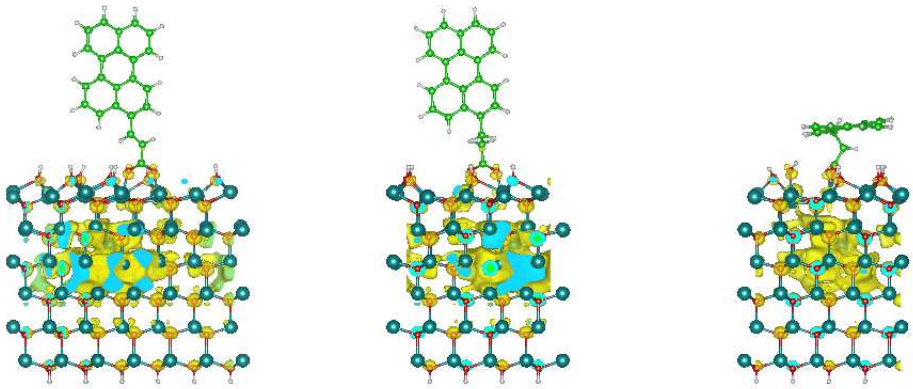

(a) (b) (c)

Figure 11: Charge-density distribution of the investigated systems with a zinc-interstitial containing ZnO surface: (a-c) **1-c**, (d-f) **2-c** and (g-i) **2′-c**. Shown are charge densities around (a, d, g) the dye-HOMO level, (b, e, h) the dye-LUMO level and (c, f, i) the dye-(LUMO+1) level.

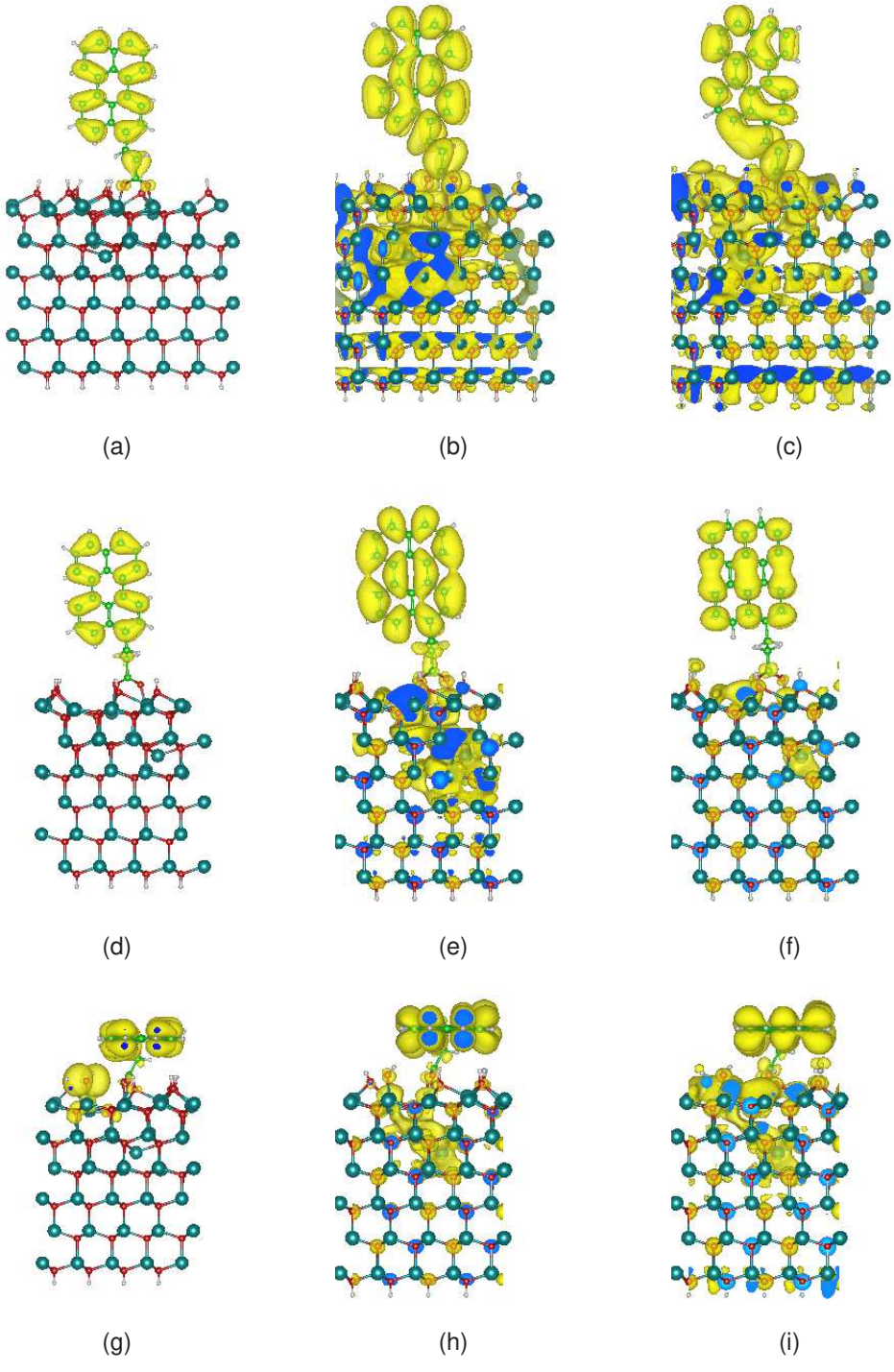

Figure 12: Population dynamics of the donor state (dye-S_1) after photoexcitation in the investigated systems: (a) **1**-ZnO, (b) **2**-ZnO and (c) **2′**-ZnO. The results are shown for the ZnO surfaces of model **a** (hydroxylated surface, solid line), model **b** (oxygen-vacancy containing surface, dashed line) and model **c** (zinc-interstitial containing surface, dotted line).

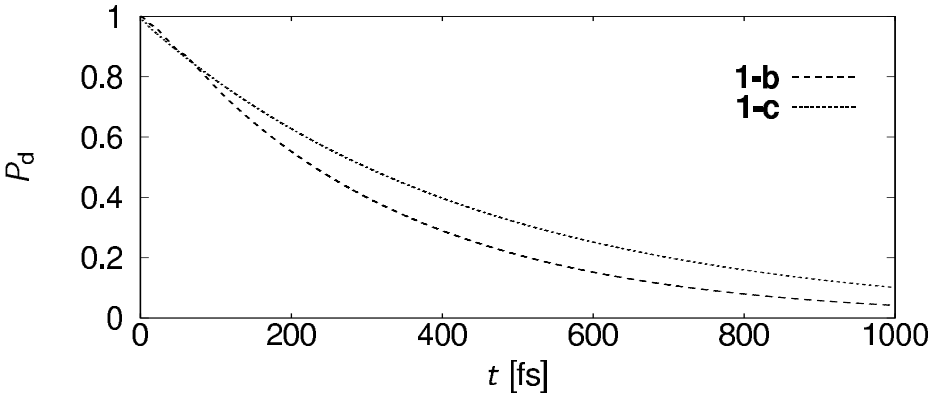

(a)

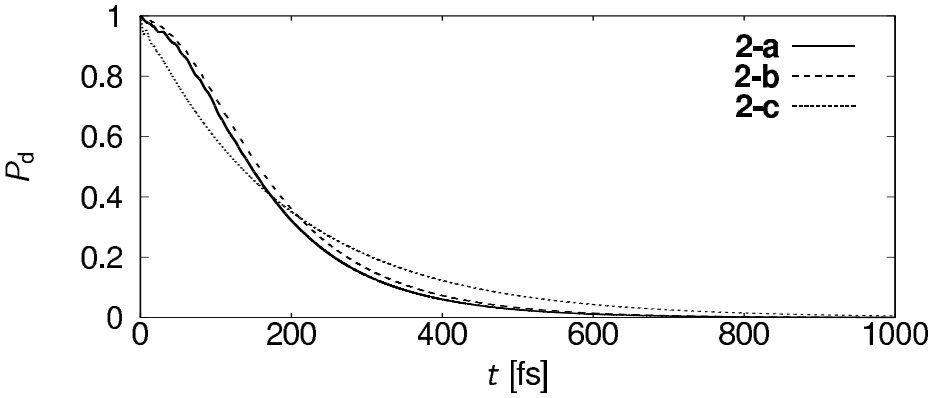

(b)

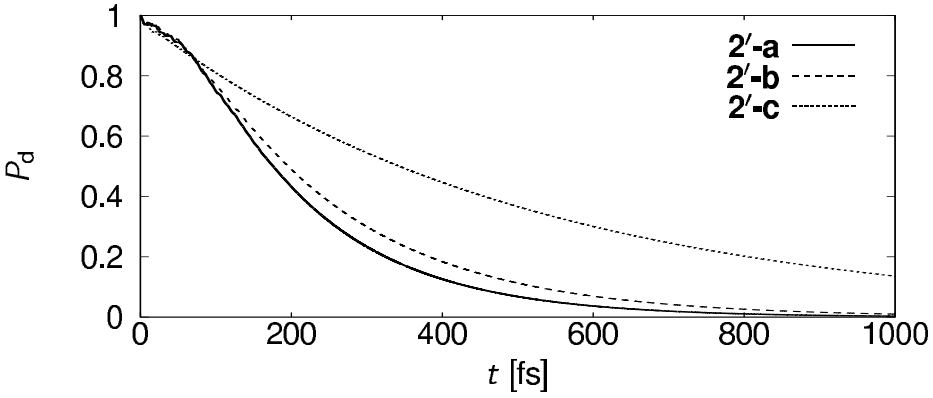

(c)

Figure 13: Population dynamics of the donor state (dye-S_2) after photoexcitation in the investigated systems: (a) **1**-ZnO, (b) **2**-ZnO and (c) **2′**-ZnO. The results are shown for the ZnO surfaces of model **a** (hydroxylated surface, solid line), model **b** (oxygen-vacancy containing surface, dashed line) and model **c** (zinc-interstitial containing surface, dotted line).

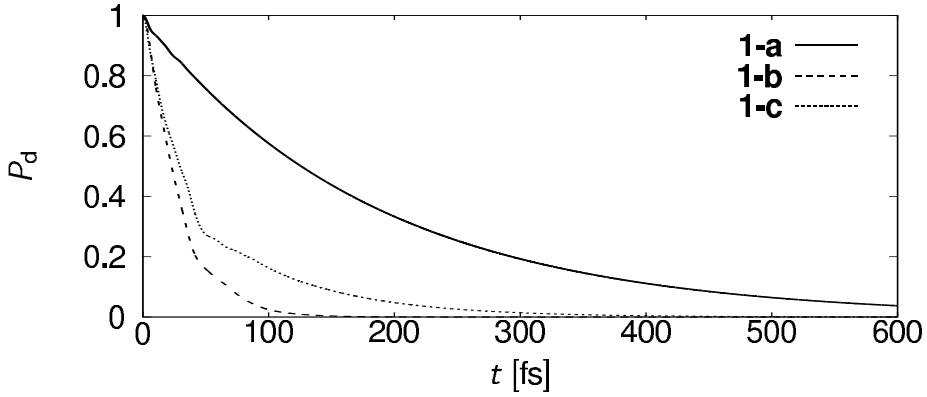

(a)

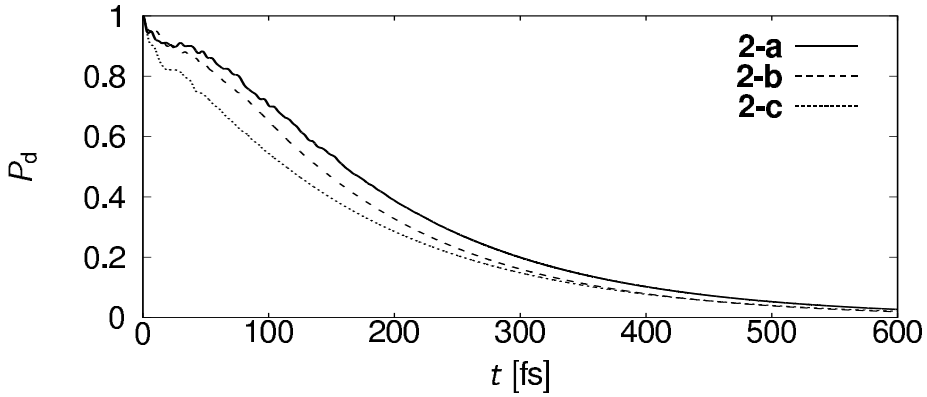

(b)

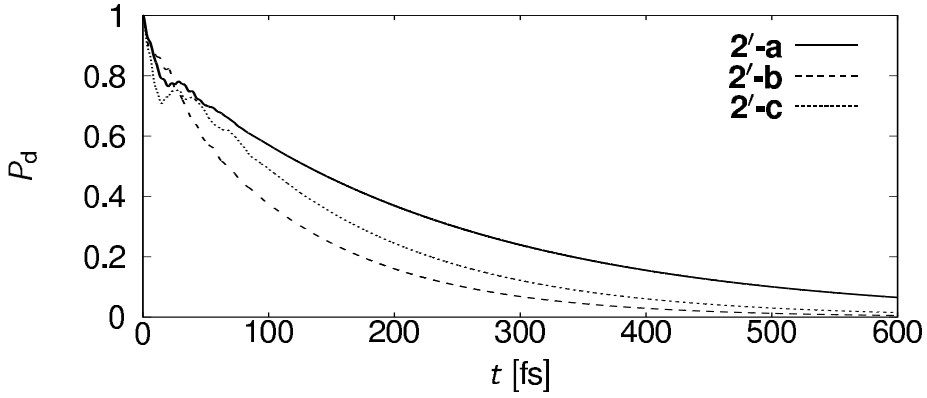

(c)

Supporting Information: Transformation between the diabatic and the adiabatic representation, test calculations for the vibronic ET dynamics and estimation of the solvation effect. This material is available free of charge via the Internet at http://pubs.acs.org.

Graphical TOC Entry